The radiative transition probabilities necessary for tracing all the downward radiative decays following excitation of O III and $3d\ ^3P_1^0$ are given by

Saraph, H. E., & Seaton, M. J. 1980, MNRAS, 193, 617.

Bhatia, A. K., & Kastner, S. O. 1993, ADNDT, 54, 133.

Froese Fischer, C. 1994, Phys. Scripta, 49, 51.

Solutions are described in

Weymann, R. J., & Williams, R. E. 1969, ApJ, 157, 1201.

Harrington, J. P., 1972, ApJ, 176, 127.

Kallman, T., & McCray, R. 1980, ApJ, 242, 615.

Elitzur, M., & Netzer, H. 1985, ApJ, 291, 646.

Netzer, H., Elitzur, M., & Ferland, G. J. 1985, ApJ, 299, 752.

Kastner, S. O., & Bhatia, A. K. 1996, MNRAS, 279, 1137.

Observations of the lines in various objects are described by

Grandi, S. A. 1980, ApJ, 238, 10.

Liu, X.-w., & Danziger, J. 1993, MNRAS 261, 463, and 262, 699.

O'Dell, C. R., & Miller, C. O. 1992, ApJ, 390, 219.

Rudy, R. J., Mazuk, S., Puetter, R. C., & Hamann, F. 2000, ApJ, 539, 166.

The He I collision strengths listed in Table 4.13 are from

Bray, I., Burgess, A., Fursa, D. V., & Tully, J. A. 2000, A&AS, 146, 481.

5

Comparison of Theory with Observations

5.1 Introduction

In the preceding three chapters much of the available theory on gaseous nebulae has been discussed, so that we are now in a position to compare it with the available observations. The temperature in a nebula may be determined from measurements of ratios of intensities of particular pairs of emission lines—those emitted by a single ion from two levels with considerably different excitation energies. Although the relative strengths of H recombination lines vary only extremely weakly with T, the ratio of the intensity of a line to the intensity of the recombination continuum varies more rapidly and can be used to measure T. Further information on the temperature may be derived from radio observations, combining long- and short-wavelength continuum observations (large and small optical depths, respectively) or long-wavelength continuum and optical-line observations. The electron density in a nebula may be determined from measured intensity ratios of other pairs of lines—those emitted by a single ion from two levels with nearly the same energy but with different radiative-transition probabilities. Likewise, measurements of relative strengths of the radio recombination lines give information on both the density and the temperature in nebulae. These methods, as well as the resulting information on the physical parameters of characteristic nebulae, are discussed in the first sections of this chapter.

In addition, information on the involved stars that provide the ionizing photons may be derived from nebular observations. For, if a nebula is optically thick to a particular type of ionizing radiation (for instance, in the H Lyman continuum), then the total number of photons of this type emitted by the star can be determined from the properties of the nebula. By combining these nebular observations, which basically measure the far-ultraviolet-ionizing radiation from the involved stars, with optical measurements of the same stars, a long base-line color index that gives information on the temperature of the stars can be determined. This scheme and the information

derived from it, about main sequence O stars and about planetary-nebula central stars, are discussed in Section 5.10.

Once the temperature and density in a nebula are known, it is fairly clear that the observed strength of a line gives information on the total number of ions in the nebula responsible for the emission of that line. Thus information is derived on the abundances of the elements in H II regions and planetary nebulae.

Each of the next ten sections of this chapter discusses a particular kind of observational analysis or diagnostic measurement of a nebula. Each method gives some specific detailed information, integrated through whatever structure there may be along the line of sight through the nebula, and also over whatever area of the nebula is covered by the analyzing device used for the observations, such as the spectrograph slit or the radio-telescope beam pattern. A more detailed comparison, in integrated form, may be made by calculating models of nebulae intended to represent their entire structure and comparing the properties of these models with observations. A discussion of these types of models, and of the progress that has been made with them, closes the chapter.

5.2 Temperature Measurements from Emission Lines

A few ions, of which [O III] and [N II] are the best examples, have energy-level structures that result in emission lines from two different upper levels with considerably different excitation energies occurring in the observable wavelength region. The energy-level diagrams of these two ions are shown in Figure 3.1, where it can be seen that, for instance, [O III] λ4363 occurs from the upper ^1S level, while λ4959 and λ5007 occur from the intermediate ^1D level. ($^3P_0$–$^1D_2$ λ4931, which can occur only by an electric–quadruple transition, has much smaller transition probability and is so weak that it can be ignored.) It is clear that the relative rates of excitation to the ^1S and ^1D levels depend very strongly on T, so the relative strength of the lines emitted by these levels may be used to measure electron temperature.

An exact solution for the populations of the various levels, and for the relative strengths of the lines emitted by them, may be carried out along the lines of the discussion in Section 3.5. However, it is simpler and more instructive to proceed by direct physical reasoning. In the low-density limit (collisional deexcitations negligible), every excitation to the ^1D level results in emission of a photon either in λ5007 or λ4959, with relative probabilities given by the ratio of the two transition probabilities, which is very close to 3 to 1. Every excitation of ^1S is followed by emission of a photon in either λ4363 or λ2321, with the relative probabilities again given by the transition probabilities. Each emission of a λ4363 photon further results in the population of ^1D, which again is followed by emission of either a λ4959 photon or a λ5007 photon; but this contribution is small in comparison with the direct excitation of ^1D and can be neglected. Thus the ratio of emission-line strengths in the low-density limit is given simply by

$$\frac{j_{\lambda4959}+j_{\lambda5007}}{j_{\lambda4363}} = \frac{\Upsilon(^3P,^1D)}{\Upsilon(^3P,^1S)}\left[\frac{A(^1S,^1D)+A(^1S,^3P)}{A(^1S,^1D)}\right]\frac{\bar{\nu}(^3P,^1D)}{\nu(^1D,^1S)}\exp(\Delta E/kT) \tag{5.1}$$

where

$$\bar{\nu}(^3P,^1D) = \frac{A(^1D_2,^3P_2)\nu(\lambda5007)+A(^1D_2,^3P_1)\nu(\lambda4959)}{A(^1D_2,^3P_2)+A(^1D_2,^3P_1)}, \tag{5.2}$$

and ΔE is the energy difference between the $^1D_2$ and $^1S_0$ levels.

Equation (5.1) is a good approximation up to $n_e \approx 10^5\ \mathrm{cm}^{-3}$. However, at higher densities collisional deexcitation begins to play a role. The lower ^1D term has a considerably longer radiative lifetime than the ^1S term, so it is collisionally deexcited at lower electron densities than ^1S, thus weakening λ4959 and λ5007. In addition, under these conditions collisional excitation of ^1S from the excited ^1D level begins to strengthen λ4363. The full statistical equilibrium Equations (3.27) can be worked out numerically for any n_e and T, but an analytic solution correct to the first order in n_e and to the first order in $\exp(-\Delta E/kT)$ is that the right-hand side of (5.1) is divided by a factor

$$f = \frac{1+\dfrac{C(^1D,^3P)C(^1D,^3P)}{C(^1S,^3P)A(^1D,^3P)}+\dfrac{C(^1D,^3P)}{A(^1D,^3P)}}{1+\dfrac{C(^1S,^3P)+C(^1S,^1D)}{A(^1S,^3P)+A(^1S,^1D)}}, \tag{5.3}$$

where

$$C(i,j) = q(i,j)n_e = 8.629\times10^{-6}\frac{n_e}{T^{1/2}}\frac{\Upsilon(i,j)}{\omega_i}\ [\mathrm{s}^{-1}].$$

Inserting numerical values of the collision strengths and transition probabilities from Chapter 3, this becomes

$$\frac{j_{\lambda4959}+j_{\lambda5007}}{j_{\lambda4363}} = \frac{7.90\exp(3.29\times10^4/T)}{1+4.5\times10^{-4}n_e/T^{1/2}}. \tag{5.4}$$

Here the representative values of the collision strengths from Table 3.6 have been used to calculate the numerical coefficients, but actually in O^{++}, there are several resonances and the resulting average collision strengths vary appreciably with temperature, so Equation (5.4) is not exact. However, in Figure 5.1 the intensity ratio is plotted (at a density of 1 cm^{-3}) using the correct collision strengths at each T, but to within the thickness of the line it is the same as the result of Equation (5.4), so very little error results from the use of mean collision strengths.

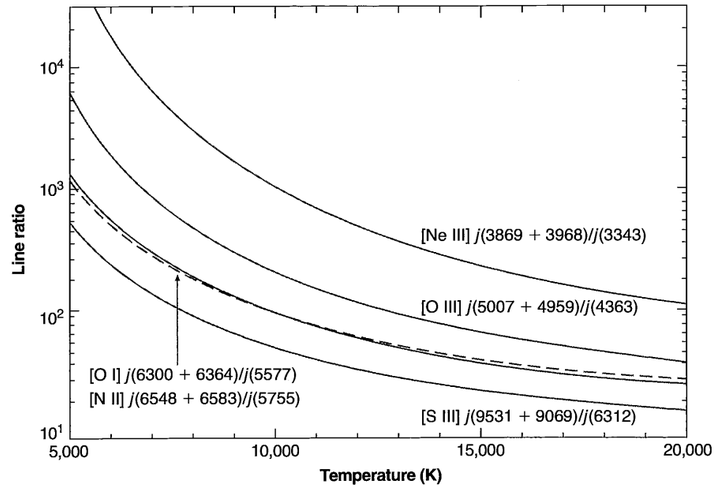

Figure 5.1

Four temperature sensitive forbidden line ratios are shown as a function of the electron temperature. The [O I] (solid line) and [N II] (dashed) ratios are nearly coincident, partially because of their similar excitation potentials. The ratios are shown in the low density limit ($n_e = 1$ cm^{-3}).

An exactly similar treatment may be carried out for [N II], [Ne III], and [S III], and the resulting equations analogous to (5.4) are

$$[\text{N II}]\frac{j_{\lambda6548} + j_{\lambda6583}}{j_{\lambda5755}} = \frac{8.23\exp(2.50 \times 10^4/T)}{1 + 4.4 \times 10^{-3} n_e/T^{1/2}} \tag{5.5}$$

$$[\text{Ne III}]\frac{j_{\lambda3869} + j_{\lambda3968}}{j_{\lambda3343}} = \frac{13.7\exp(4.30 \times 10^4/T)}{1 + 3.8 \times 10^{-5} n_e/T^{1/2}} \tag{5.6}$$

$$[\text{S III}]\frac{j_{\lambda9532} + j_{\lambda9069}}{j_{\lambda6312}} = \frac{5.44\exp(2.28 \times 10^4/T)}{1 + 3.5 \times 10^{-4} n_e/T^{1/2}} \tag{5.7}$$

These equations form the basis for optical temperature determinations in gaseous nebulae. Since the nebulae are optically thin in forbidden-line radiation, the ratio of the integrals of the emission coefficients along a ray through the nebula is observed directly as the ratio of emergent intensities, so if the nebula is assumed to be isothermal and to have sufficiently low density that the low-density limit is applicable, the temperature is directly determined. Alternatively, the ratio of the fluxes

from the whole nebula may be measured in the case of smaller nebulae. No information need be known on the distance of the nebula, the amount of O^{++} present, and so on, as all these factors cancel out. If collisional deexcitation is not completely negligible, even a rough estimate of the electron density substituted into the correction term in the denominator provides a good value of T. The observed strengths of the lines must be corrected for interstellar extinction, but this correction is usually not too large because the temperature-sensitive lines are relatively close in wavelength.

The [O III] line-intensity ratio ($\lambda4959 + \lambda5007$)/$\lambda4363$ is quite large and is therefore rather difficult to measure accurately. Although $\lambda\lambda4959$, 5007 are strong lines in many gaseous nebulae, $\lambda4363$ is relatively weak, and furthermore is close to Hg I $\lambda4358$, which unfortunately is becoming stronger and stronger in the spectrum of the sky due to increasing light pollution. Large intensity ratios are difficult to measure accurately, and reasonably precise temperature measurements therefore require carefully calibrated photoelectric measurements with fairly high-resolution spectral analyzers. Most of the early work centered on the [O III] lines, partly because they occur in the blue spectral region in which detectors are most sensitive, and partly because [O III] is quite bright in typical high-surface brightness planetary nebulae. The [N II] lines are stronger in the outer parts of H II regions, where the ionization is lower and the O mostly emits [O II] lines. A great deal of more recent work has used all of these lines.

The $^2D^o$ and $^2P^o$ levels of [O II] and [S II] have different excitation potentials, and lines that originate from these two levels can also be used as temperature indicators. These have the advantage of lying in spectral regions that are relatively easy to observe, but the lines are widely separated in wavelength so the correction for interstellar extinction is larger. All of these temperature indicators are shown in Figure 5.1.

Let us first examine optical determinations of the temperatures in H II regions, some selected results of which are collected in Figure 5.2, which compares temperatures determined by several of the line ratios mentioned above. Note that in this and other figures, the observed intensity ratio has been corrected for interstellar extinction in the way outlined in Chapter 7, and the temperature has been computed using the methods described in this book.

It can be seen that all the temperatures of these H II regions are in the range 7,000–14,000 K. A good part of the dispersion in temperature is due to physical differences between the H II regions. As we shall see in Chapter 10, within a galaxy the abundances of the heavy elements tend to increase inward, resulting in the differences in temperatures shown in the figure.

Planetary nebulae have higher surface brightness than typical H II regions, and as a result there is a good deal more observational material available for planetaries, particularly [O III] determinations of the temperature. Most planetaries are so highly ionized that [N II] is relatively weak, but measurements of it are also available. A selection of the best observational material is collected in Figure 5.3, which shows that the temperatures in the hottest planetary nebulae are typically

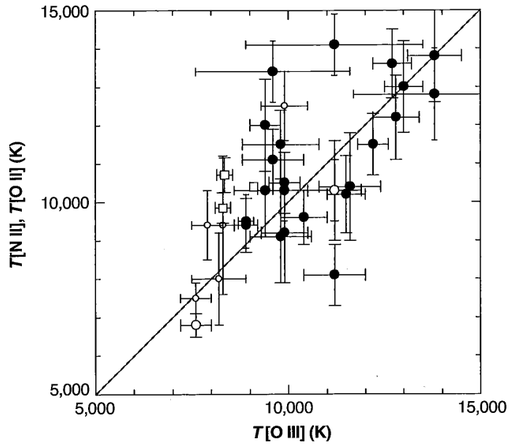

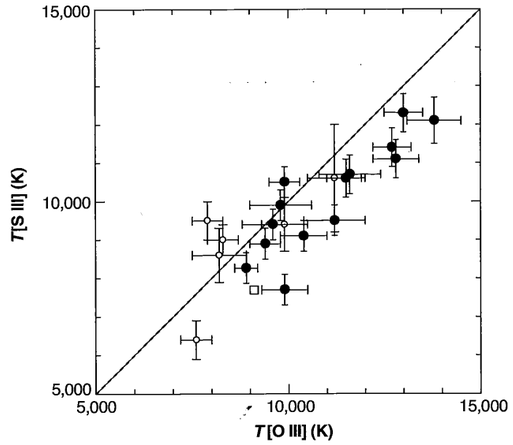

Figure 5.2
A comparison of values of the temperature in H II regions. The closed circles are H II regions in M 101; the open circles, in NGC 2403; and the open squares, different locations in the Orion Nebula.

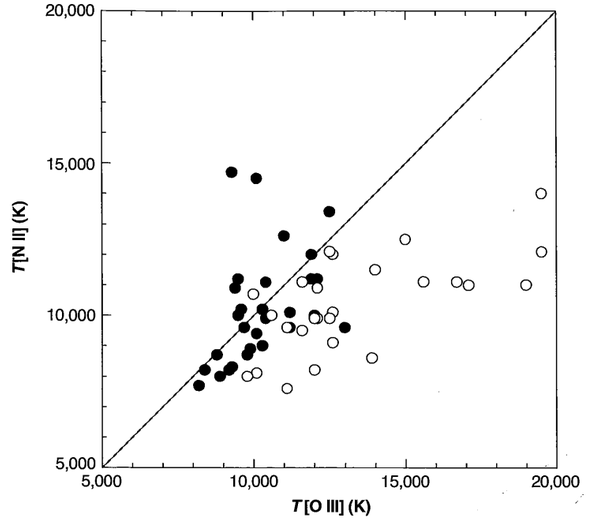

Figure 5.3
A comparison of two temperature indicators for a sample of planetary nebulae.

somewhat higher than in H II regions. This is partly a consequence of higher effective temperatures of the central stars in planetary nebulae (to be discussed in Section 5.8), leading to a higher input of energy per photoionization, and partly a consequence of the higher electron densities in typical planetaries, resulting in collisional deexcitation and decreased efficiency of radiative cooling. Like the H II regions, some of the dispersion is due to physical differences among the nebulae. Some are halo objects with relatively low heavy-element abundances, as discussed in Chapter 10, and the lower cooling efficiency results in somewhat above-average temperatures.

From Figures 5.2 and 5.3, it is reasonable to adopt $T \approx 10{,}000$ K as an order-of-magnitude estimate for any nebula with near-normal abundances; with somewhat greater precision we may adopt representative values $T \approx 9{,}000$ K in the brighter parts of an H II region, and $T \approx 11{,}000$ K in a typical bright planetary nebula.

Another method that can be used to determine the temperature in a nebula is to compare the relative strength of a collisionally excited line, such as C III] λ1909, with a recombination line of the next lower state of ionization, such as C II λ4267, since both depend on the product of densities $n(C^{++})n_e$, which therefore cancels out of their ratios. Figure 5.4 shows a few of these types of ratios as a function of

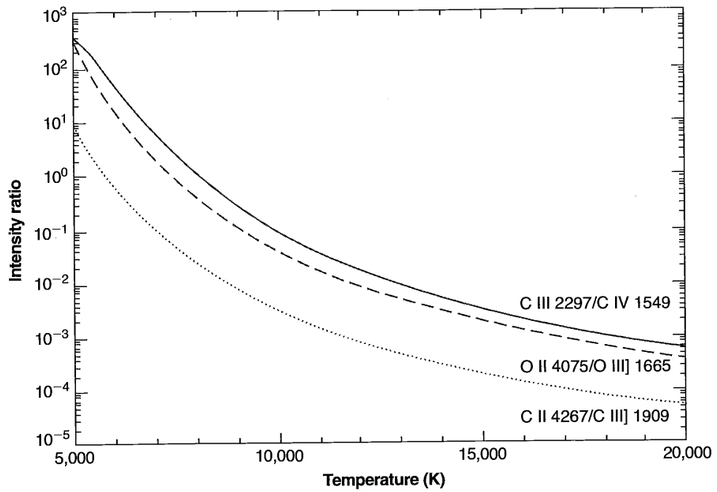

Figure 5.4
Several temperature-sensitive line-intensity ratios of dielectronic recombination to collisionally excited lines.

T. This method has been applied to relatively few objects because the collisionally excited line usually occurs in the vacuum ultraviolet and it is difficult to obtain space-borne observations. There is the additional complication that a significant correction may be necessary if the spectrometers used for the different lines also have different entrance apertures since these are spatially extended objects. But the method has the advantage that the observed ratio is a very powerful function of the temperature, so that even modest signal-to-noise spectra can determine the temperature quite accurately.

5.3 Temperature Determinations from Optical Continuum Measurements

Although it might be thought that the temperature in a nebula could be measured from the relative strengths of the H lines, in fact their relative strengths are almost independent of temperature, as Table 4.4 shows. The physical reason for this behavior is that all the recombination cross sections to the various levels of H have approximately the same velocity dependence, so the relative numbers of atoms formed by captures to each level are nearly independent of T, and since the cascade matrices depend only

on transition probabilities, the relative strengths of the lines emitted are also nearly independent of T. These calculated relative line strengths are in good agreement with observational measurements.

However, the temperature in a nebula can be determined by measuring the relative strength of the recombination continuum with respect to a recombination line. Physically, the reason this ratio does depend on the temperature is that the emission in the continuum (per unit frequency interval) depends on the width of the free-electron velocity-distribution function—that is, on T.

The theory is straightforward, for we may simply use Table 4.4 to calculate the H-line emission, and Tables 4.7–4.9 and 4.12 to calculate the continuum emission, and thus find their ratio as a function of T. Figure 5.5 plots the calculated ratios for two choices of the continuum. The first is near H$\beta\lambda$4861 and includes the H I recombination and two-photon continua as well as the He I recombination continuum. [A nebula with $n(\mathrm{He}^+) = 0.08n(\mathrm{H}^+)$ and $n(\mathrm{He}^{++}) = 0$ has been assumed, but any other abundances or ionization conditions determined from line observations of the nebula could be used.] The second choice is the Balmer discontinuity, $j_\nu(\lambda3646-)$–$j_\nu(\lambda3646+)$, which eliminates everything except the H I recombination continuum due to recaptures into $n = 2$. [The He II recombination, of course, would also contribute if $n(\mathrm{He}^{++}) \neq 0$ since recaptures to its $n = 4$ level produce light at this wavelength.] Note that the λ4861 continuum has been calculated in the limit $n_p \to 0$ (no collisional deexcitation of H I $2\,^2S$ and hence maximum relative strength of the H I two-photon continuum) and also for the case $n_p = 10^4$ cm^{-3}, $n(\mathrm{He}^+) = 10^3$ cm^{-3}, taking account of collisional deexcitation, while the Balmer discontinuity results are independent of density and $n(\mathrm{He}^+)$.

The continuum at λ4861 is made up chiefly of the H I Paschen and higher-series continua, whose sum increases slowly with T, and the two-photon continuum, whose strength decreases slowly with T; the sum hence is roughly independent of T, and the ratio of this continuum to Hβ therefore increases with T. On the other hand, the strength of the Balmer continuum at the series limit decreases approximately as $T^{-3/2}$, and its ratio to Hβ therefore decreases slowly with T, as Figure 5.5 shows.

The observations of the continuum are difficult because it is weak and can be seriously affected by weak lines. High-resolution spectrophotometric measurements with high-sensitive detectors are necessary. To date the most accurate published data seem to be measurements of the Balmer continuum, which is considerably stronger than the Paschen continuum near Hβ. A difficulty in measuring the Balmer continuum, of course, is that the higher Balmer lines are crowded just below the limit, so the intensity must be measured at longer wavelengths and extrapolated to λ3646+. Furthermore, continuous radiation emitted by the stars involved in the nebulae and scattered by interstellar dust may have a sizable Balmer discontinuity, which is difficult to disentangle from the true nebular recombination Balmer discontinuity. Some of the best published results for H II regions and planetary nebulae are collected in Figure 5.6, which shows that the temperatures measured by this method are generally somewhat smaller than the temperatures for the same objects measured from forbidden-line ratios. These discrepancies will be discussed again in the next section

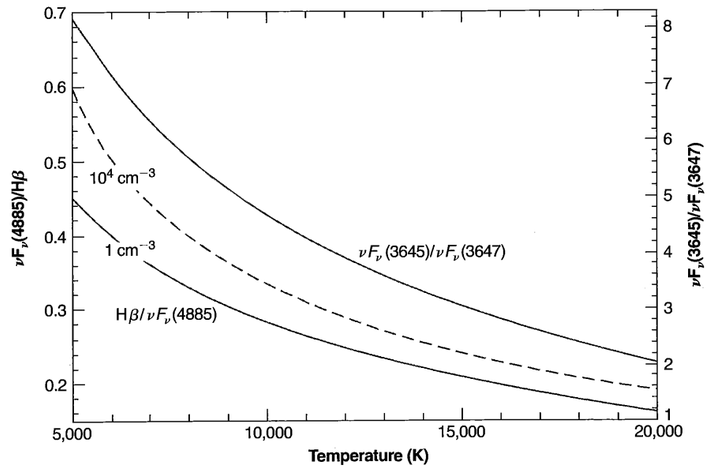

Figure 5.5

Two temperature-sensitive ratios involving hydrogen lines or continua. The upper curve is the ratio of fluxes above and below the Balmer limit. The lower curves show the flux in the continuum just redward of Hβ relative to Hβ. Two densities are shown, a low density in which two-photon emission occurs after every capture to $2\,^2S$, and a higher density at which collisions to $2\,^2P^o$ weaken the two-photon continuum. All continua include a contribution from He^+, assuming that all He is in the form of He^+ and a helium abundance corresponding to He/H = 0.08 by number.

following the discussion of temperature measurements from the radio-continuum observations.

5.4 Temperature Determinations from Radio-Continuum Measurements

Another completely independent temperature determination can be made from radio-continuum observations. The idea is quite straightforward—namely, that at sufficiently low frequencies any nebula becomes optically thick, and therefore, at these frequencies (assuming an isothermal nebula) the emergent intensity is the same as that from a blackbody—the Planck function $B_\nu(T)$; or equivalently, the measured brightness temperature is the temperature within the nebula,

$$T_{b\nu} = T\left[1 - \exp(-\tau_\nu)\right] \rightarrow T \quad \text{as } \tau_\nu \rightarrow \infty \tag{5.8}$$

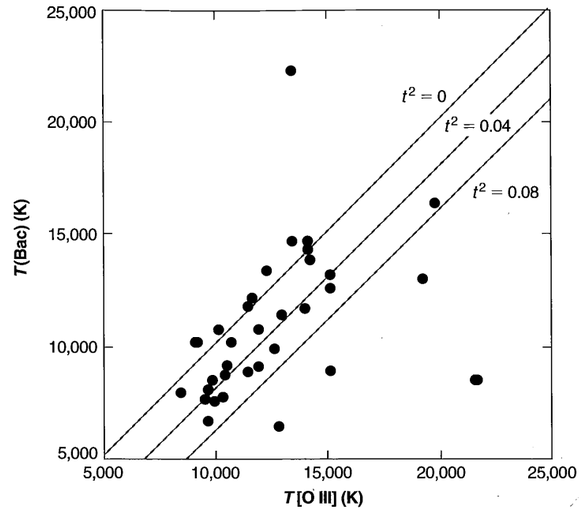

Figure 5.6

Comparison of the [O III] and Balmer continuum temperatures for a sample of planetary nebulae. The upper line indicates the expected correlation in the absence of temperature fluctuations, and the two lower lines give the correlation for two values of t^2.

as in Equation (4.37). Note that if there is background non-thermal synchrotron radiation (beyond the nebula) with brightness temperature T_{bg_ν} and foreground radiation (between the nebula and the observer) with brightness temperature T_{fg_ν}, this equation becomes

$$T_{b\nu} = T_{fg\nu} + T\left[1 - \exp\left(-\tau_\nu\right)\right] + T_{bg\nu}\exp\left(-\tau_\nu\right) \rightarrow T_{fg\nu} + T \quad \text{as } \tau_\nu \rightarrow \infty \tag{5.9}$$

(assuming no foreground absorption).

The difficulty with applying this method is that at frequencies that are sufficiently low that the nebulae are optically thick ($\nu \approx 3 \times 10^8$ Hz or $\lambda \approx 10^2$ cm for many dense nebulae), even the largest radio telescopes have beam sizes that are comparable to or larger than the angular diameters of typical H II regions. Therefore, the nebula does not completely fill the beam, and a correction must be made for the projection of the nebula onto the antenna pattern.

The antenna pattern of a simple parabolic or spherical dish is circularly symmetric about the axis, where the sensitivity is at a maximum. The sensitivity decreases outward in all directions, and in any plane through the axis it has a form much like

a Gaussian function with angular width of order λ/d, where d is the diameter of the telescope. The product of the antenna pattern with the brightness-temperature distribution of the nebula then gives the mean brightness temperature, which is measured by the radio-frequency observations. The antenna pattern thus tends to broaden the nebula and to wipe out much of its fine structure. To determine the temperature of a nebula that is small compared with the width of the antenna pattern, it is therefore necessary to know its angular size accurately. But, of course, no nebula really has sharp outer edges, inside which it has infinite optical depth and outside which it has zero optical depth. In a real nebula, the optical depth decreases more or less continuously but with many fluctuations, from a maximum value somewhere near the center of the nebula to zero just outside the edge of the nebula, and what is really needed is the complete distribution of optical depth over the face of the nebula.

This can be obtained from high radio-frequency measurements of the nebula, for in the high-frequency region, the nebula is optically thin, and the measured brightness temperature gives the product $T\tau_1$,

$$T_{b1} = T\left[1 - \exp\left(-\tau_1\right)\right] \rightarrow T\tau_1 \text{ as } \tau_1 \rightarrow 0, \tag{5.10}$$

as in Equation (4.37). (In the remainder of this section, the subscript 1 is used to indicate a high frequency, and the subscript 2 is used to indicate a low frequency.) At high frequencies, the largest radio telescopes have considerably better angular resolution than at low frequencies because of the smaller values of λ/d, so that if the nebula is assumed to be isothermal, the high-frequency measurements can be used to prepare a map of the nebula, giving the product $T\tau_1$ at each point. Thus for any assumed T, the optical depth τ_1/τ_2 is determined at each point from the high-frequency measurements. The ratio of optical depths, τ_1/τ_2, is known from Equation (4.31), so τ_2 can be calculated at each point, and then the expected brightness temperature T_{b2} can be calculated at each point:

$$T_{b2} = T\left[1 - \exp\left(-\tau_2\right)\right]. \tag{5.11}$$

Integrating the product of this quantity with the antenna pattern gives the expected mean brightness temperature at the low frequency. If the assumed T is not correct, this expected result will not agree with the observed mean brightness temperature, and another assumed temperature must be tried until agreement is reached. This, then, is a procedure for correcting the radio-frequency continuum measurements for the effects of finite beam size at low frequencies.

A few of the most accurate available radio-frequency measurements of temperature in H II regions are collected in Table 5.1. Many of the observations were obtained with single-dish telescopes, and so had limited spatial resolution. At 408 MHz, most of the nebulae listed have central optical depths $\tau_2 \approx 1$ to 10, while at 85 MHz, the optical depths are considerably larger. At lower frequencies the beam size of the antenna is larger and in addition the background (non-thermal) radiation is larger, so many of the nebulae are measured in absorption at this lower frequency. A few objects have been observed with the Very Large Array (VLA) at 330 MHz, with a spatial resolution

Table 5.1
Radio and optical temperature determinations in H II regions

Object	Radio continuum (K)	Radio recombination (K)	Optical (K)
M42	$7{,}875 \pm 360$	8,500	8800
M43	$9{,}000 \pm 1{,}700$	6,700	
NGC 2024	$8{,}400 \pm 1{,}000$	8,200	
W51	$7{,}800 \pm 300$	7,500	
W43	$5{,}410 \pm 300$	5,640	
M17	$7{,}600 \pm 400$	$9{,}100 \pm 100$	
NGC 6334	7,000	7,000	
NGC 6357	6,900	7,300	

References for table: Shaver et al. 1983, MNRAS, 204, 53; Subrahmanyan, R., & Goss, W. M. 1996, MNRAS, 281, 239; and papers cited therein.

of roughly 1 arc minute. The radio continua give temperatures that are fairly consistent with other independent ways of measuring the mean temperature in a nebula.

Exactly the same method can be used to measure the temperatures in planetary nebulae, but as they are very small in comparison with the antenna beam size at the frequencies at which they are optically thick, the correction for this effect is quite important. Nearly all the planetary nebulae are too small for mapping at even the shortest radio-frequency wavelengths with single-dish radio telescopes, but it is possible to use the surface brightness in a hydrogen recombination line such as Hβ, since it is also proportional to the proton emission measure, the integral

$$I(\mathrm{H}\beta) \propto \int n_p n_e \, ds = E_p, \tag{5.12}$$

to get the relative values of τ_2 at each point in the nebula. Even the optical measurements have finite angular resolution because of the broadening effects of seeing. Then, for any assumed optical depth of the nebula at one point and at one frequency, the optical depths at all other points and at all frequencies can be calculated. For any assumed temperature, the expected flux at each frequency can thus be calculated and compared with the radio measurements, which must be available for at least two (and preferably more) frequencies, one in the optically thin region and one in the optically thick region. The two parameters T and the central optical depth must be varied to get the best fit between calculations and measurements. The uncertainties are largely due to the lack of accurate optical isophotes, from which the distribution of brightness temperature over the nebula must be calculated.

With the Very Large Array (VLA) radio interferometer it is possible to achieve angular resolution as small as $0.05''$ at high frequency ($\lambda = 1.3$ cm), ideal for these measurements. Mean temperatures determined in this way for planetary nebulae include $T = 8{,}300$ K for NGC 6543, $T = 18{,}500$ K for IC 418, and $T = 14{,}000$ K

for NGC 7027. The high-resolution radio images, obtained at these high frequencies, provide excellent information on the spatial structure of planetary nebulae.

5.5 Temperature Determinations from Radio and UV Absorption Lines

The H I 21-cm line occurs as an electron spin–flip transition, with a transition probability of $A = 2.85 \times 10^{-15}$ s^{-1}. The calculation of A is exactly analogous to atomic transition probabilities but here it involves coupling of I, the nuclear spin of the proton, with J, the angular momentum of the electron. The latter is made up of spin (non-zero) and orbital (zero) angular momenta to form F, the total spin of nucleus plus electron. It is an allowed magnetic dipole transition in these variables, but has a very small transition probability because of the ν^3 dependence of A.

Observations of 21-cm absorption, together with Lα absorption, can measure the excitation temperature T_{ex} of the hyperfine structure levels that produce the 21 cm line. T_{ex}, often referred to as the spin temperature in radio-astronomy papers, is defined in terms of the level populations as

$$\frac{n_u}{n_l} = \frac{\omega_u}{\omega_l} \exp(-\chi_{ul}/kT_{ex})$$

where χ_{ul} is the excitation energy of the line and the n's and ω's are the populations and statistical weights of the lower and upper levels.

T_{ex} is equal to the gas kinetic temperature if the level populations are determined mainly by collisions. This is usually the case when the electron density is above the critical density of the transition, and the radiation density at the frequencies which can populate and depopulate the upper level are low. Collisions with electrons and hydrogen atoms are the most important. At temperatures of 10^3 K and 10^4 K, the downward collisional rate coefficients are $q_{10} = 2.4 \times 10^{-10}$ and 5.2×10^{-10} cm^3 s^{-1} for collisions with hydrogen atoms, and 6.0×10^{-9} and 7.9×10^{-9} cm^3 s^{-1} for collisions with electrons. The corresponding critical electron density is 3.6×10^{-7} cm^{-3}, so the level populations are collisionally dominated for most conditions. Scattering by Lα photons can alter the level populations, and this can be important under some conditions. However, the assumption that $T_{ex}(21\,\text{cm}) = T_e$ is often a good approximation.

The line optical depth τ of any transition is given by

$$\tau = \kappa L = a(n_l - n_u\omega_l/\omega_u)L \tag{5.13}$$

where κ is the line opacity, L is the path length, and a is the atomic absorption cross section (cm^2). The first term in parentheses represents direct absorption of radiation from the lower level, while the second term corrects for stimulated emission.

Using the definition of T_{ex}, the opacity κ can be written as

$$\kappa = an_l\left[1 - \exp\left(-\chi_{ul}/kT_{ex}\right)\right] \text{ [cm}^{-1}\text{]}$$

There are two limiting forms to this equation. If $\chi_{ul} \gg kT_{ex}$, the limit that holds for Lα at $T \sim 10^4$ K, the exponential can be ignored and the opacity is given by

$$\kappa_{UV} = a_{UV}n_l.$$

The opposite limit occurs for H I 21 cm. Here $\chi_{ul} \ll kT_{ex}$ and the exponent can be expanded as $\exp(-\chi_{ul}/kT_{ex}) \approx 1 - \chi_{ul}/kT_{ex}$. Then, the opacity is given by

$$\kappa_{radio} = a_{radio}n_l\frac{\chi_{ul}}{kT_{ex}}$$

i.e., in this case it is proportional to the ratio n/T_{ex} and not n itself. So, 21-cm absorption is strongly weighted to colder regions.

The ratio of the optical depths of the H I 21 cm and Lα lines can be combined to measure the excitation temperature.

$$\frac{\tau_{radio}}{\tau_{UV}} = \frac{n_{l,radio}}{n_{l,UV}}\frac{\kappa_{radio}L}{\kappa_{UV}L} = \frac{n_{l,radio}}{n_{l,UV}}\frac{a_{radio}}{a_{UV}}\frac{\chi_{ul}}{kT_{ex}}.$$

For the particular case of 21 cm and Lα this becomes

$$\frac{\tau_{21\text{cm}}}{\tau_{\text{L}\alpha}} = \frac{1}{4}\frac{a_{21\text{cm}}}{a_{\text{L}\alpha}}\frac{\chi_{ul}}{kT_{ex}} = \frac{1}{4}\frac{A_{21\text{cm}}\lambda_{21\text{cm}}^3}{A_{\text{L}\alpha}\lambda_{\text{L}\alpha}^3}\frac{\chi_{ul}}{kT_{ex}} = 3.84 \times 10^{-7}T_{ex}^{-1}.$$

The factor of $\frac{1}{4}$ enters if the hyperfine structure levels that produce 21 cm absorption have populations that are proportional to their statistical weight, since both levels absorb Lα while only the lower level absorbs 21 cm.

5.6 Electron Densities from Emission Lines

The average electron density in a nebula may be measured by observing the effects of collisional deexcitation. This can be done by comparing the intensities of two lines of the same ion, emitted by different levels with nearly the same excitation energy so that the relative excitation rates to the two levels depend only on the ratio of collision strengths. If the two levels have different radiative transition probabilities or different collisional deexcitation rates, the relative populations of the two levels will depend on the density, and the ratio of intensities of the lines they emit will likewise depend on the density. The best examples of lines that may be used to measure the electron density are [O II] λ3729/λ3726, and [S II] λ6716/λ6731, with energy-level diagrams shown in Figure 5.7.

The relative populations of the various levels and the resulting relative line-emission coefficients may be found by setting up the equilibrium equations for the populations of each level as described in Section 3.5. However, direct physical reasoning easily shows the effects involved. Consider the example of [O II] in the low-density limit $n_e \to 0$, in which every collisional excitation is followed by emission

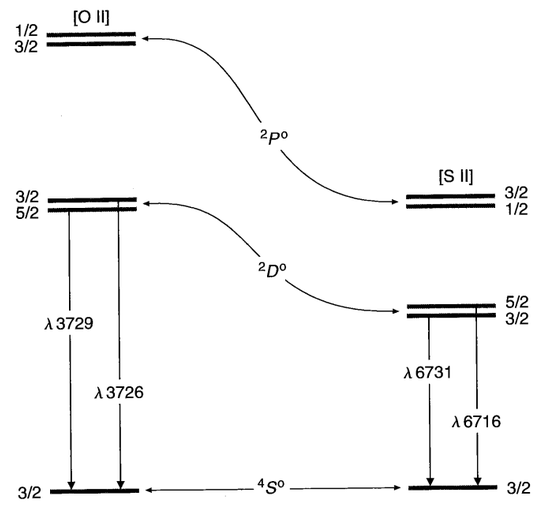

Figure 5.7
Energy-level diagrams of the $2p^3$ ground configuration of [O II] and $3p^3$ ground configuration of [S II].

of a photon. Since the relative excitation rates of the $^2D_{5/2}$ and $^2D_{3/2}$ levels are proportional to their statistical weights [see Equation (3.22)], the ratio of strengths of the two lines is $j_{\lambda 3729}/j_{\lambda 3726} = 1.5$. On the other hand, in the high-density limit, $n_e \to \infty$, collisional excitations and deexcitations dominate and set up a Boltzmann populations ratio. Thus, the relative populations of the two levels $^2D_{5/2}$ and $^2D_{3/2}$ are in the ratio of their statistical weights, and therefore the relative strengths of the two lines are in the ratio

$$\frac{j_{\lambda 3729}}{j_{\lambda 3726}} = \frac{n(^2D^o_{5/2})}{n(^2D^o_{3/2})}\frac{A_{\lambda 3729}}{A_{\lambda 3726}} = \frac{3}{2}\frac{3.6 \times 10^{-5}}{1.6 \times 10^{-4}} = 0.34$$

The transition between the high- and low-density limits occurs in the neighborhood of the critical densities [see Equation (3.30)], which are $n_e \approx 3 \times 10^3$ cm^{-3} for $^2D^o_{5/2}$ and $n_e \approx 1.6 \times 10^4$ cm^{-3} for $^2D^o_{3/2}$. The full solution of the equilibrium equations, which also takes into account all transitions, including excitation to the $^2P^o$ levels with subsequent cascading downward, gives the detailed variation of intensity ratio with the electron density that is plotted in Figure 5.8. Note from the collisional transition rates that the main dependence of this ratio is on $n_e/T^{1/2}$. There is also a very slight

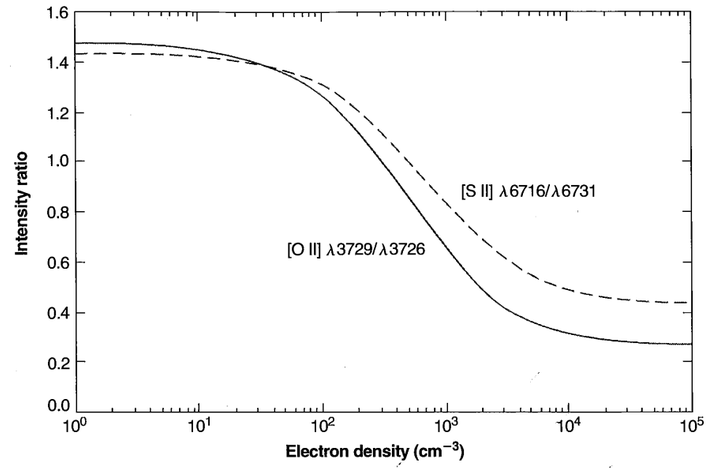

Figure 5.8
Calculated variation of [O II] (*solid line*) and [S II] (*dashed line*) intensity ratios as functions of n_e at T = 10,000 K. At other temperatures the plotted curves are very nearly correct if the horizontal scale is taken to be $n_e(10^4/T)^{1/2}$.

temperature dependence (as a consequence of the cascading from $^2P^o$) that cannot be seen on this graph.

An exactly similar treatment holds for [S II]; the calculated ratio $j_{\lambda 6716}/j_{\lambda 6731}$ is also shown in Figure 5.8. Other pairs of lines from ions with the same type of structure, which may also be used for measuring electron densities, are [N I], [Cl III], [Ar IV], and [K V] in the optical region, as well as [Ne IV] λλ2422, 2424 in the vacuum ultraviolet.

From the observational point of view, it is unfortunate that the [O II] λλ3726, 3729 are so close in wavelength; a spectrograph, spectrometer, or interferometer with good wavelength resolution must be used to separate the lines. However, a fair amount of data is available on both H II regions and planetary nebulae.

Table 5.2 compares some densities measured in H II regions. It can be seen that typical densities in several H II regions are of order $n_e \approx 10^2$ cm^{-3}. (NGC 1976 M is a position in the outer part of the Orion Nebula.) Several H II regions have dense condensations in them, though—for instance, the central part of the Orion Nebula, near the Trapezium (NGC 1976 A), with λ3729/λ3726 = 0.50, corresponding to $n_e \approx 3.0 \times 10^3$ cm^{-3}. In fact, observations of the [O II] ratio at many points in NGC 1976, of which only A and M are listed in Table 5.2, show that the mean electron density is highest near the center of the nebula and decreases relatively smoothly outward in

Table 5.2
Electron densities in H II regions

Object	$I(\lambda3729)/I(\lambda3726)$	n_e (cm^{-3})
NGC 1976 A	0.5	3.0×10^3
NGC 1976 M	1.26	1.4×10^2
M 8 Hourglass	0.67	1.6×10^3
M 8 Outer	1.26	1.5×10^2
MGC 281	1.37	70
NGC 7000	1.38	60

all directions. The three-dimensional structure of the nebula thus presumably must have a density maximum, and the intensity ratio observed at the center results from emission all along the line of sight, so the actual central density must be higher than 4.5×10^3 cm^{-3}. A model can be constructed that approximately reproduces all the measured [O II] ratios in NGC 1976; this model has $n_e \approx 1.7 \times 10^4$ cm^{-3} at the center and decreases to $n_e \approx 10^2$ cm^{-3} in the outer parts. Furthermore, measurements of the [S II] ratio at many points in the inner bright core of NGC 1976 (about 8′ diameter) show good agreement between the electron densities determined from the [S II] lines and the [O II] lines. Similarly, in M 8 the [O II] measurements show that the density falls off outward from the Hourglass, a small dense condensation in which $n_e \approx 2 \times 10^3$ cm^{-3}.

Some information on electron densities in planetary nebulae derived from [O II] and [S II] is shown in Figure 5.9, in which the densities derived from these two ions are mostly within a factor of two of each other. In most planetaries the degree of ionization is high, and most of the [O II] and [S II] lines that arise in fairly low stages of ionization are emitted either in the outermost parts of the nebula or in the densest parts, where recombination depresses the ionization the most. Thus the densities derived from these ions may not be representative of the entire nebula. The higher stages of ionization, [Ar IV], [K V], and so on, are more representative, but their lines are weaker and more difficult to measure. An example is NGC 7662, for which the [Ar IV] lines give $n_e = 1.0 \times 10^4$ cm^{-3}, while the [Ne IV] pair at λλ2422, 2424 give 9.6×10^3 cm^{-3}, both at an assumed $T = 10^4$ K.

The electron densities derived from these line ratios may be used in Equations (5.4) and (5.5) to correct the observations of the temperature-sensitive lines of [O III] and [N II] for the slight collisional deexcitation effect; and actually these corrections have already been taken into account in Tables 5.1 and 5.2. Though the electron density derived from [O II] line measurements may not exactly apply in the [O III] emitting region, the density effect is small enough that an approximate correction should be satisfactory.

In the densest planetaries known, collisional deexcitation of [O III] $^1D_2$ is strong enough that the $(\lambda4959 + \lambda5007)/\lambda4363$ ratio is significantly affected. The best example is IC 4997, with $\lambda3729/\lambda3726 = 0.34$, corresponding to n_e poorly determined in the high-density limit but certainly greater than 10^5 cm^{-3}. The measured $(\lambda4959 + \lambda5007)/\lambda4363 \approx 22$, which would correspond to $T \approx 4 \times 10^4$ K if there were no collisional deexcitation. This temperature is far too large to be understood from the known heating and cooling mechanisms in photoionization equilibrium, and the ratio is undoubtedly strongly affected by collisional deexcitation. If it is assumed that $T \approx 12{,}000$ K, the [O III] ratio gives $n_e \approx 10^6$ cm^{-3}; higher assumed temperatures correspond to somewhat lower electron densities, and vice versa.

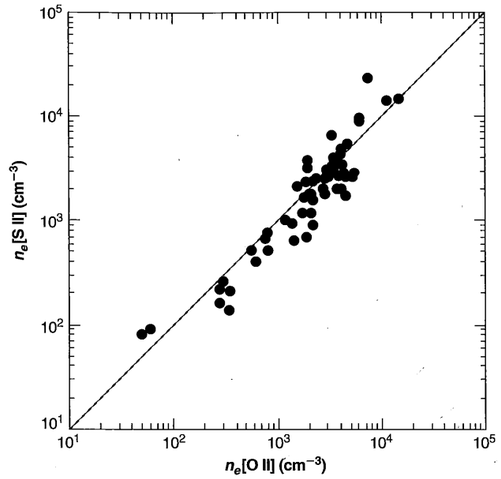

Figure 5.9
Densities of a sample of planetary nebulae calculated from the [O II] and [S II] line ratios described in the text.

Transitions with higher critical densities can be used as diagnostics in denser environments. The ion C III, whose energy-level diagram is shown in Figure 5.10, has two observed emission lines, [C III] $3s^2\ ^1S_0$–$3s\ 3p\ ^3P^o_2$ λ1907, a highly forbidden magnetic quadrupole transition, and C III $3s^2\ ^1S_0$–$3s\ 3p\ ^3P^o_1$ λ1909, an intercombination or "semi-forbidden" electric–dipole transition. The two lines therefore have a ratio of intensities fixed in the low-density limit by collision strengths alone. It is approximately $I(^1S_0$–$^3P^o_2)/I(^1S_0$–$^3P^o_1) \approx 5/3$ by Equation (3.22), but more nearly exactly = 1.53, because the downward radiative transition $^1S_0$–$^3P^o_0$ is completely forbidden; hence collisional excitation of $^3P^o_0$ is always followed by a further collisional process, either deexcitation to $^1S_0$, or excitation to $^3P^o_1$ or $^3P^o_2$. In the high-density limit, on the other hand, the ratio is fixed by the ratio of statistical weights and transition probabilities, and $\approx 9 \times 10^{-5}$. The detailed form of its variation with electron density is shown in Figure 5.11.

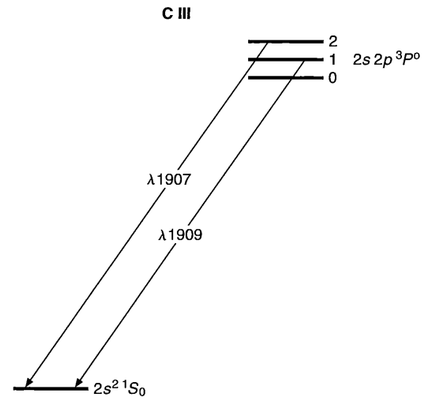

Figure 5.10
Energy-level diagram of lowest terms of C III $2s^2$ and $2s2p$ configurations, and resulting C III] and [C III] emission lines. The splitting within the $2s2p\ ^3P^o$ term is exaggerated in this diagram.

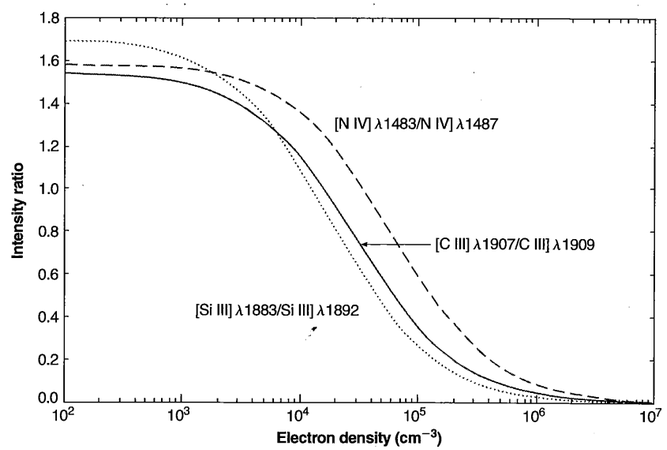

Figure 5.11
Calculated variation of [C III] λ1907/C III] λ1909, [N IV] λ1483/N IV] λ1487, and [Si III] λ1883 / Si III] λ1892 intensity ratios as a function of electron density n_e at T = 10,000 K.

The λ1907/λ1909 ratio has mainly been measured for bright planetary nebulae. They mostly have ratios in the range 0.8 to 1.4, corresponding to $n_e = 3 \times 10^4$ to 3×10^3 cm^{-3}. The large, low-density nebulae like NGC 650/1, 3587, 6720, 6853, and 7293 are too faint to have yet been measured in these lines. But the small, high-surface-brightness planetary IC 4997 has λ1907/λ1909 ≈ 0.03, showing that its mean electron density $n_e \approx 10^6$ cm^{-3}, agreeing quite well with the [O III] results.

5.7 Electron Temperatures and Densities from Infrared Emission Lines

Sensitive infrared detectors, together with airborne or orbiting telescopes that are above most of the infrared absorption in the Earth's atmosphere, have made it possible to measure "fine-structure" lines such as [O III] $^3P_0$–$^3P_1$ λ88 μm and $^3P_1$–$^3P_2$ λ52 μm (see Figure 3.1 and Table 3.12). These far-infrared lines have much smaller excitation potentials than the optical lines such as $^3P_2$–$^1D_2$ λ5007. Thus a ratio like $j_{\lambda 5007}/j_{\lambda 88\mu m}$ depends strongly on temperature but, since the $^3P_2$ level has a much lower critical electron density than $^1D_2$ does, the ratio depends on density also. On the other hand, the ratio $j_{\lambda 52\mu m}/j_{\lambda 88\mu m}$ hardly depends on temperature at all (since both excitation potentials are so low in comparison with typical nebular temperatures), but does depend strongly on density (since the two upper levels have different critical densities). Hence by measuring two [O III] ratios, we can determine the average values of the two parameters, T and n_e. Figure 5.12 shows calculated curves of the values of the two [O III] intensity ratios for various values of temperature and electron density. Observed values of the line ratios are entered on the diagram for several planetary nebulae, from which the average T and n_e can be immediately read off. They agree reasonably well with values determined independently from optical lines alone. Including the infrared lines makes determinations of temperature and density possible for many more ions than the optical lines. The chief difficulty, given an airborne telescope and spectrograph, is to be certain that exactly the same area is measured in both spectral regions. For this reason the measurements available to date are chiefly for entire planetary nebulae.

5.8 Electron Temperatures and Densities from Radio Recombination Lines

Information can be obtained on the temperature and density in gaseous nebulae from measurements of the radio recombination lines. Practically all the observational results refer to H II regions, which have considerably larger fluxes than planetary nebulae and hence can be much more readily observed with radio telescopes. The populations of the high levels of H depend on T and n_e, as explained in Section 4.4, and the strengths of the lines emitted by these levels relative to the continuum and to one another therefore depend on n_e, T, and the optical depth, which is conventionally expressed in terms of the emission measure E defined in Equation (4.32). Comparison of measured and calculated relative strengths thus can be used to calculate mean values of n_e, T, and E.

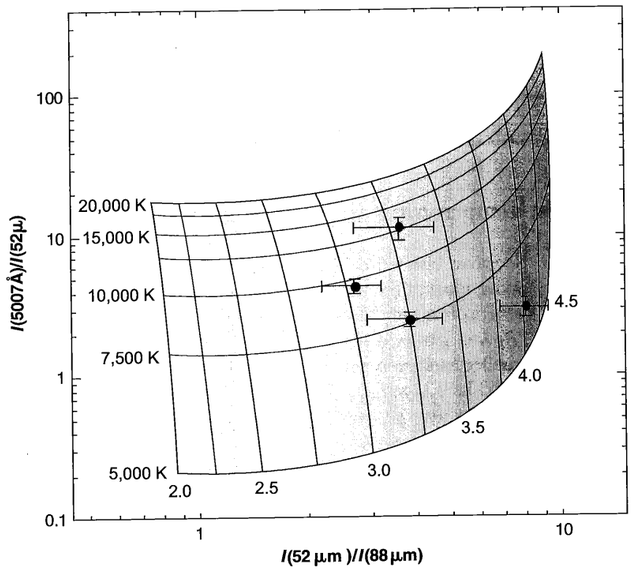

Figure 5.12
Calculated variation of [O III] forbidden-line relative intensity ratios as functions of T (5,000 K to 20,000 K) and the log of the electron density n_e. Observed planetary-nebula ratios plotted with an indication of probable errors.

To calculate the expected strengths, we must solve the equation of radiative transfer, since the maser effect is often important, as was shown in Section 4.4. Furthermore, the continuum radiation is not weak in comparison with the line radiation and therefore must be included in the equation of transfer. The observations are generally reported in terms of brightness temperature. We will use T_C for the measured temperature in the continuum near the line and $T_L + T_C$ for the measured brightness temperature at the peak of the line (see Figure 5.13), so that T_L is the excess brightness temperature due to the line.

We will consider an idealized homogeneous isothermal nebula. The optical depth in the continuum, which we will write τ_C, is given by Equation (4.32). The optical depth in the center of the line is

$$\tau_{cL} = \tau_L + \tau_C \tag{5.14}$$

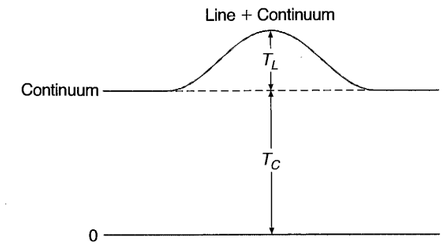

Figure 5.13
A radio-frequency line superimposed on the radio-frequency continuum, showing the brightness temperatures at the center of the line and in the nearby continuum; T_L and T_C, respectively.

where τ_L is the contribution from the line alone,

$$d\tau_L = \kappa_L ds$$

and

$$\kappa_L = n_n k_{0L}. \tag{5.15}$$

Here we consider a n, Δn line between an upper level $m = n + \Delta n$ and a lower level n; the central line-absorption cross section, corrected for stimulated emission as in Equation (4.43), is

$$\begin{aligned}\kappa_{0L} &= \frac{\omega_m}{\omega_n}\frac{\lambda^2}{8\pi^{3/2}\Delta\nu_D}A_{m,n}\left[1 - \frac{b_m}{b_n}\exp(-h\nu/kT)\right] \\ &= \frac{\omega_m}{\omega_n}\frac{\lambda^2(\ln 2)^{1/2}}{4\pi^{3/2}\Delta\nu_L}A_{m,n}\left[1 - \frac{b_m}{b_n}\exp(-h\nu/kT)\right]\end{aligned} \tag{5.16}$$

In this equation a Doppler profile has been assumed, with $\Delta\nu_D$, the half width at e^{-1} of maximum intensity and $\Delta\nu_L$ the full-width at half-maximum intensity, the conventional quantity used in radio astronomy. Combining (5.16) with

$$n_m = b_n n^2 \left(\frac{h^2}{2\pi mkT}\right)^{3/2}\exp(X_n/kT)n_p n_e\ [\mathrm{cm}^{-3}] \tag{5.17}$$

and using $\exp(X_n/kT) \approx 1$ to a good approximation for all observed radio-frequency recombination lines, expressing $A_{m,n}$ in terms of the corresponding f-value, f_{nm}, and expanding the stimulated-emission correction as in Equation (4.43) gives, for the

special case of local thermodynamic equilibrium ($b_m = b_n = 1$, which we shall denote by an asterisk throughout this section),

$$\begin{aligned}\tau_L^* &= 1.53 \times 10^{-9} \frac{n^2 f_{nm} \nu}{\Delta\nu_L T^{2.5}} E_p \\ &= 1.01 \times 10^{7} \frac{\Delta n\, f_{nm}}{n \Delta\nu_L T^{2.5}} E_p.\end{aligned} \tag{5.18}$$

The proton-emission measure, defined in Equation (5.12), is expressed in cm^{-6} pc in both forms of Equation (5.18), and

$$\nu = \frac{\nu_0}{n^2} - \frac{\nu_0}{m^2} \approx \frac{2\nu_0 \Delta n}{n^3}.$$

In the true nebular case,

$$\begin{aligned}\tau_L &= \tau_L^* b_n \frac{\left[1 - \dfrac{b_m}{b_n} \exp(-h\nu/kT)\right]}{\left[1 - \exp(-h\nu/kT)\right]} \\ &= \tau_L^* b_m \left(1 - \frac{kT}{h\nu} \frac{d \ln b_n}{dn} \Delta n\right)\end{aligned} \tag{5.19}$$

by the power-series expansion, while the continuum optical depth is the same as in thermodynamic equilibrium, because the free electrons have a Maxwellian distribution.

Now we will use these expressions and the formal solution of the equation of transfer to calculate the ratio of brightness temperatures $r = T_L/T_C$ in the special case of thermodynamic equilibrium,

$$\begin{aligned}r^* &= \frac{T_L + T_C}{T_C} - 1 = \frac{T\left[1 - \exp\left(-\tau_{CL}\right)\right]}{T\left[1 - \exp\left(-\tau_C\right)\right]} - 1 \\ &= \frac{1 - \exp\left[-\left(\tau_L^* + \tau_C\right)\right]}{1 - \exp\left(-\tau_C\right)} - 1.\end{aligned} \tag{5.20}$$

If $\tau_L^* \ll 1$ (this is a good approximation in all lines observed to date), and in addition, $\tau_C \ll 1$ (this is generally but not always a good approximation),

$$r^* = \frac{\tau_L^*}{\tau_C}.$$

Under the assumption of local thermodynamic equilibrium, the observed ratio of brightness temperatures in line and continuum thus gives (in the limit of small optical

depth) the ratio of optical depths, which, in turn, from Equations (4.32) and (5.18), measures T. Note that the continuum emission measure E_c, given by

$$E_c = \int n_+ n_e ds, \tag{5.21}$$

involves all positive ions, but the proton emission measure E_p involves only H^+ ions, so their ratio depends weakly on the helium abundance, which, however, is reasonably well known. This scheme was used in the early days of radio recombination-line observations to determine the temperatures in H II regions, but it is not correct because in a nebula the deviations from thermodynamic equilibrium are significant, as is shown by the fact that measurements of different lines in the same nebula, when reduced in this way, give different temperatures.

To calculate the brightness–temperature ratio $r = T_L/T_C$ in the true nebular case, we note that the brightness temperature in the continuum is still given by

$$T_C = T\left[1 - \exp\left(-\tau_C\right)\right].$$

However, both the line-emission and line-absorption coefficients differ from their thermodynamic equilibrium values. The line-emission coefficient depends on the population in the upper level, so

$$j_L = j_L^* b_m,$$

while the line-absorption coefficient, as shown in Equation (5.19), is

$$\kappa_L = \kappa_L^* b_m \beta,$$

where

$$\beta = 1 - \frac{kT}{h\nu} \frac{d \ln bn}{dn} \Delta n. \tag{5.22}$$

The equation of transfer, in intensity units is

$$\frac{dI_\nu}{d\tau_{CL}} = -I_\nu + \frac{j_L + j_C}{\kappa_L + \kappa_C} = -I_\nu + S_\nu, \tag{5.23}$$

where

$$\begin{aligned}S_\nu &= \frac{j_L^* b_m + j_C}{\kappa_L^* b_m \beta + \kappa_C} \\ &= \frac{\kappa_L^* b_m + \kappa_C}{\kappa_L^* b_m \beta + \kappa_C} B_\nu(T)\end{aligned} \tag{5.24}$$

from Kirchhoff's law, so that the brightness temperature at the center of the line is

$$T_L + T_C = \left[\frac{\kappa_L^* b_m + \kappa_C}{\kappa_L^* b_m \beta + \kappa_C}\right] T \left\{1 - \exp\left[-\left(b_m \beta \tau_L^* + \tau_C\right)\right]\right\} \tag{5.25}$$

Hence finally,

$$r = \frac{T_L}{T_C} = \left[\frac{\kappa_L^* b_m + \kappa_C}{\kappa_L^* b_m \beta + \kappa_C}\right]\left[\frac{1 - \exp\left(-b_m \beta \tau_L^* + \tau_C\right)}{1 - \exp\left(-\tau_C\right)}\right] - 1, \tag{5.26}$$

which depends only on one optical depth, say τ_C, the ratio of optical depths, $\tau_L^*/\tau_C = \kappa_L^*/\kappa_C$ given by Equations (4.42) and (5.14), and the b_n factors, which, in turn, depend on n_e and T.

Thus, when the deviations from thermodynamic equilibrium are taken into account, r depends not only on T, but also on n_e and τ_C (or equivalently, E). Therefore, observations of several different lines in the same nebula are necessary to determine T, n_e, and E from measurements of radio-frequency recombination lines. The procedure is to make the best possible match between all measured lines in a given nebula, and the theoretical calculations for a given T, n_e, and E, using the $b_n(T, n_e)$ calculations described in Chapter 4. There are observational problems connected with the fact that the radio recombination lines, coming as they do from levels with large n and thus large atomic radii, suffer significant impact broadening even at the low densities of nebulae. This makes the wings of the line difficult to define observationally except with very good signal-to-noise ratio data. Otherwise significant contributions from the wings may easily be overlooked. Another problem is that measurements are made at different frequencies and with different radio telescopes, so the antenna beam patterns are not identical for all lines. Model calculations show that over a wide range of nebular conditions, measurements of lines with $\Delta n = 1$ at frequencies near 10 GHz (such as 109α at 5.009 GHz) are only slightly affected by maser effects and by deviations from thermodynamic equilibrium, and therefore are especially suitable for determining nebular temperatures. Data on some of the best observed nebulae are collected in Figure 5.14, which compares the recombination line measurements with temperatures determined from collisionally excited lines. The temperatures determined from the recombination lines tend to be lower than those determined from collisionally excited lines, as was also found with the Balmer jump and radio continuum.

The range in temperatures is largely due to physical differences among the nebulae. Radio techniques have the advantage that nebulae can be detected at large distances within the galactic plane, where interstellar extinction prevents optical spectroscopy. The measured temperatures show a clear increase with increasing distance from the center, which is consistent with the decrease in heavy-element abundance outward from the center that we shall discuss in Chapter 10.

Average electron densities can also be found from the radio recombination line measurements. The best procedure is to compare lines of two different frequencies,

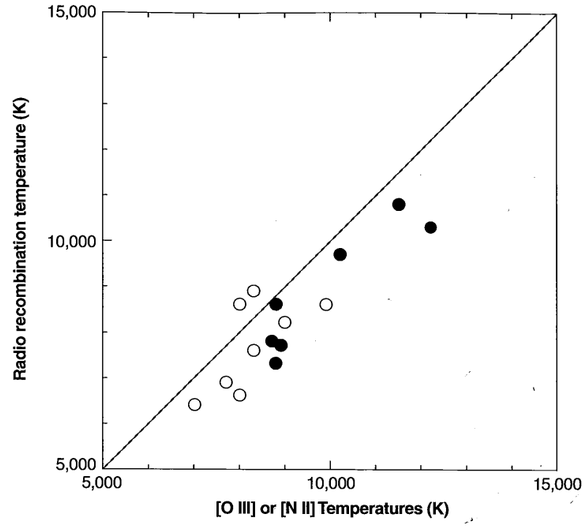

Figure 5.14
A comparison between temperatures determined from optical forbidden lines ([O III] filled circles; [N II] open circles) and radio recombination lines.

such as 85α and 109α, or 66α and 85α. Naturally it is important to match the antenna beam widths as closely as possible. Very high n lines cannot be used, because impact (Stark) broadening becomes important, making the wings difficult to define and measure accurately. The mean electron density derived in this way for the Orion Nebula, NGC 1976, $n_e = 2.4 \times 10^3$ cm^{-3}, is comparable with an emission-weighted average of the [O II] determinations. Likewise, radio recombination line measurements for a few of the highest surface brightness planetary nebulae give mean electron densities ranging from $n_e = 8.5 \times 10^3$ cm^{-3} in NGC 6543 to 1.6×10^5 cm^{-3} in NGC 7027.

5.9 Filling and Covering Factors

Direct photographs of nearly all planetaries and H II regions show chaotic structure to some degree. In some cases nebulae appear to have large hollow central regions. As we shall see in the next chapter, these can be understood as resulting from a highly ionized, low-density, high-velocity "wind," flowing out from the central star or stars. In other

cases large departures from spherical symmetry are present, with significant regions being relatively free of matter. These density condensations, low-density hollows, etc., are an important feature of the structure of gaseous nebulae.

They can be detected quantitatively if the densities derived from [O II] line ratios in a large, well resolved nebula of known distance, such as NGC 1976, are used to predict the expected high-frequency radio continuum brightness temperature, by combining Equations (4.32) and (4.37) and assuming that the nebula is spherically symmetric. They give, in the limit of small optical depth, which is a good approximation for high-frequency observations,

$$T_{b\nu} = 8.24 \times 10^{-2} T^{-0.35} \nu^{-2.1} E_c \tag{5.27}$$

with the continuum emission measure E_c given by Equation (5.21), with units in cm^{-6} pc. Note that the predicted brightness temperature depends only very weakly on the nebular temperature.

The measured values of $T_{b\nu}$ are invariably smaller than those predicted in this way, typically by a factor of order ten. This can only be understood if the nebula is thinner along the line of sight than perpendicular to it (which is actually the case for the Orion nebula, as we shall see), or in terms of density fluctuations. The line-ratio density measurements are heavily weighted toward the regions of strongest emission—that is, of highest density. These measured densities thus deviate greatly from the average density along a typical path or ray through the nebula. Fluctuations in density must be taken into account in describing the structure of the nebula.

The simplest, though extreme, way to do so is to idealize the nebula as containing gas in small clumps or condensations, with electron density n_e within the condensations, but with zero electron density between them. The "filling factor" ε is then the fraction of the total volume occupied by the condensations. The space between the condensations, in this simple picture, is a vacuum, which makes no contribution to the emission, mass, opacity, etc., of the nebula. The filling factor may be assumed to be constant throughout a nebula, for simplicity, or it can be allowed to vary with position, to match either an image or the spectrum of the real nebula. For NGC 1976, assuming a constant filling factor, the comparison of density and radio-continuum measurements gives $\varepsilon = 0.03$, and values ranging from 0.01 to 0.5 or so have been determined for other H II regions and planetary nebulae.

The covering factor, $\Omega/4\pi$, is the fraction of 4π sr that is covered by gas, as viewed from the location of the central star. The covering factor takes into account regions where the gas is either nonexistent or has insufficient column density to fully absorb the ionizing continuum, and so appear fainter.

Note that under the filling-factor and covering-factor description of nebulae the intensity of an emission is given by

$$I_l = \int j_l \, ds = \int \varepsilon \, n_i n_e \varepsilon_l(T) \, ds; \tag{5.28}$$

the luminosity in the same line, integrated over the volume of the nebula, is

$$L_l = \frac{\Omega}{4\pi} \int \varepsilon \, n_i n_e \varepsilon_l(T) \, dT \tag{5.29}$$

the number of recombinations is

$$Q(\text{H}^0) = \frac{\Omega}{4\pi} \frac{4\pi}{3} r_1^3 \varepsilon \, n_p n_e \alpha_B(\text{H}^0) \tag{5.30}$$

replacing Equation (2.19) or

$$Q(\text{H}^0) = \frac{\Omega}{4\pi} \int_0^{r_1} \varepsilon \, n_p n_e \alpha_B(\text{H}^0) \, dV, \tag{5.31}$$

replacing its analogue in Section 5.10, and the total mass of H in the nebula is

$$M_{\text{H}} = m_{\text{H}} \frac{\Omega}{4\pi} \int_0^{r_1} \varepsilon \, n_p \, dV \tag{5.32}$$

Likewise the radial optical depth becomes

$$\tau_\nu(r) = \int_0^r \varepsilon \, n(\text{H}^0, r') a_\nu \, dr' \tag{5.33}$$

replacing Equation (2.12). Similar generalizations can be made in other equations, always on the basis that n stands for the density in the condensations, which are assumed to fill a fraction ε of the total volume, with vacuum (or hot, low-density invisible gas) between them.

5.10 Ionizing Radiation from Stars

Observations of gaseous nebulae may be used to find the number of ionizing photons emitted by a star and thus to determine a long base-line color index for it between the Lyman ultraviolet region and an ordinary optical region, from which the effective temperature of the star can be derived. The idea of the method is quite straightforward. If the nebula around the star is optically thick in the Lyman continuum, it will absorb all the ionizing photons emitted by the star. Thus the total number of ionizations in the nebula per unit time is just equal to the total number of ionizing photons emitted per unit time, and since the nebula is in equilibrium, these ionizations are just balanced by the total number of recaptures per unit time, so

$$\int_{\nu_0}^{\infty} \frac{L_\nu}{h\nu} d\nu = Q(\text{H}^0) = \int_0^{r_1} n_p n_e \alpha_B(\text{H}^0, T) \, dV,$$

where L_ν is the luminosity of the star per unit frequency interval. In this and the following equations we have set the covering and filling factors to unity, but these

could easily be included following the discussion in the previous section. Note that by using the recombination coefficient α_B, we have included the ionization processes due to diffuse ionizing photons emitted in recaptures within the nebula—see Equation (2.19). The luminosity of the entire nebula in a particular emission line, say Hβ, also depends on recombinations throughout its volume:

$$L(\mathrm{H}\beta) = \int_0^{r_1} 4\pi j_{\mathrm{H}\beta}\, dV$$
$$= h\nu_{\mathrm{H}\beta} \int_0^{r_1} n_p n_e \alpha^{eff}_{\mathrm{H}\beta}(\mathrm{H}^0, T)\, dV$$

Thus, dividing

$$\frac{\dfrac{L(\mathrm{H}\beta)}{h\nu_{\mathrm{H}\beta}}}{\displaystyle\int_{\nu_0}^{\infty} \frac{L_\nu}{h\nu} d\nu} = \frac{\displaystyle\int_0^{r_1} n_p n_e \alpha^{eff}_{\mathrm{H}\beta}(\mathrm{H}^0, T)\, dV}{\displaystyle\int_0^{r_1} n_p n_e \alpha_B(\mathrm{H}^0, T)\, dV} \tag{5.34}$$
$$\approx \frac{\alpha^{eff}_{\mathrm{H}\beta}(\mathrm{H}^0, T)}{\alpha_B(\mathrm{H}^0, T)}$$

gives the result that the number of photons emitted by the nebula in a specific recombination line such as Hβ is directly proportional to the number of photons emitted by the star with $\nu \geq \nu_0$. Note that the proportionality between the number of ionizing photons absorbed and the number of line photons emitted does not depend on any assumption about constant density, and that replacing the ratio of integrals by the ratio of recombination coefficients is a good approximation because $\alpha^{eff}_{\mathrm{H}\beta}/\alpha_B$ depends only weakly on T. Note further that any other emission line could have been used instead of Hβ, or alternatively the radio-frequency continuum emission at any frequency at which the nebula is optically thin could have been used, except that then the ratio of nebular photons emitted to ionizing photons would involve the ratio of the number of protons to the total number of positive ions, which depends weakly on the He abundance. The number of ionizing photons may be compared with the luminosity of the star at a particular frequency ν_f in the observable region,

$$\frac{L_{\nu_f}}{\displaystyle\int_{\nu_0}^{\infty} \frac{L_\nu}{h\nu}\, d\nu} = \frac{L_{\nu_f}}{\dfrac{L(\mathrm{H}\beta)}{h\nu_{\mathrm{H}\beta}}} \frac{\dfrac{L(\mathrm{H}\beta)}{h\nu_{\mathrm{H}\beta}}}{\displaystyle\int_{\nu_0}^{\infty} \frac{L_\nu}{h\nu}\, d\nu} \tag{5.35}$$
$$= h\nu_{\mathrm{H}\beta} \frac{\alpha^{eff}_{\mathrm{H}\beta}(\mathrm{H}^0, T)}{\alpha_B(\mathrm{H}^0, T)} \frac{\pi F_{\nu_f}}{\pi F_{\mathrm{H}\beta}}$$

where the ratio of luminosities has been expressed in terms of the ratio of the observed fluxes at the earth from the star at ν_f and from the nebula at Hβ. This ratio is independent of the distance, and is in addition independent of the interstellar extinction if the nebula and the star are observed at the same effective wavelength by choosing $\nu_f = \nu_{\mathrm{H}\beta}$.

It is often more convenient to make the stellar measurements with a fairly wide filter of the type ordinarily used for photometry (for instance, the V filter of the UBV system), and we can then write a similar equation in terms of

$$L_V = \int_0^{\infty} s_\nu\,(V)\, L_\nu\, d\nu$$

and

$$\pi F_V = \int_0^{\infty} s_\nu\,(V) \pi F_\nu\, d\nu,$$

where $s_\nu(V)$ is the sensitivity function of the telescope-filter-photocell combination, known from independent measurements. For measurements of stars in bright nebulae, it is advantageous to use a narrower-band filter that isolates a region in the continuum between the brightest nebular emission lines, to minimize the correction for the "sky" background. In principle, any observable frequency ν_f can be used, and likewise any observable recombination line, for instance Hα, might be measured instead of Hβ. The method of using the nebular observations to measure the stellar ultraviolet radiation was first proposed by Zanstra, who assumed that the flux from a star could be approximately represented by the Planck function $B_\nu(T_*)$, so that

$$\frac{L_{\nu f}}{\displaystyle\int_{\nu_0}^{\infty} \frac{L_\nu}{h\nu} d\nu} = \frac{B_{\nu f}(T_*)}{\displaystyle\int_{\nu_0}^{\infty} \frac{B_\nu(T_*)}{h\nu} d\nu}$$

and the measurements thus determine T_*, the so-called Zanstra temperature of a star that ionizes a nebula. However, modern theoretical work on stellar atmospheres shows that there are important deviations between the emergent fluxes from stars and Planck functions, particularly in the regions where there are large changes in opacity with frequency, such as at the Lyman limit itself and at the various limits, due to other ions at shorter wavelengths, so that it is not a very good approximation to set $F_\nu = B_\nu(T_*)$. As illustrations, Figures 5.15 and 5.16 show calculated models for stars with $T_* = 40{,}000$ K, $\log g = 4$, approximately an O6 main-sequence star, and $T_* = 100{,}000$ K, $\log g = 6$, a fairly typical planetary-nebula star. Thus the ratios

$$\frac{L_{\nu_f}}{\displaystyle\int_{\nu_o}^{\infty} \frac{L_\nu}{h\nu} d\nu} = y(T_*) = \frac{\pi F_\nu(T_*, g)}{\displaystyle\int_{\nu_0}^{\infty} \frac{\pi F_\nu(T_*, g)}{h\nu} d\nu} \tag{5.36}$$

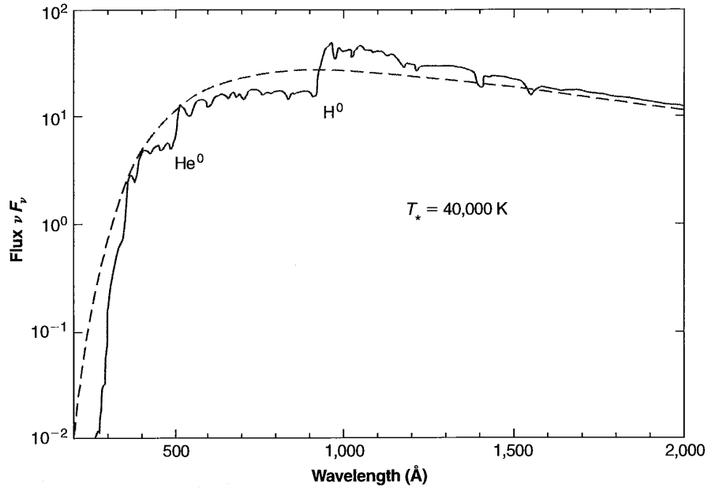

Figure 5.15
Calculated flux from a model O6 star with $T_* = 40{,}000$ K, log $g = 4$ (*solid line*), compared with blackbody flux for the same effective temperature (*dashed line*). The ionization edges of atomic hydrogen and helium are marked.

should be determined from the best available sequences of model stellar atmospheres, and it can be seen that there is a one-parameter relationship $y = y(T_*)$ for a fixed value of g or along a fixed line in the T_*, log g plane.

We shall first use these relationships to examine the effective temperatures of population I O stars in H II regions, and then generalize these equations and use them to describe the higher-temperature planetary-nebula central stars.

Many H II regions are observed, but a fairly large fraction of them contain several O stars that contribute to the ionization and thus complicate the determination of the effective temperature of individual stars. The best cases for measurement are clearly nebulas with only a single involved hot star. Furthermore, the basic assumption of the method is that the nebula completely absorbs the stellar ionizing radiation and is a true Strömgren sphere (radiation-bounded rather than density-bounded). It is difficult to be certain that this assumption is fulfilled in any particular nebula, though well-defined ionization fronts at the outer edge of a nebula suggest that it is and thus indicate that it is a good candidate to be measured. However, as we shall see in Chapter 7, absorption of ionizing photons by dust can still cause serious errors in the results.

Today a large body of optical, infrared, and radio-frequency measurements are available. The infrared and radio measurements have the advantage that they are

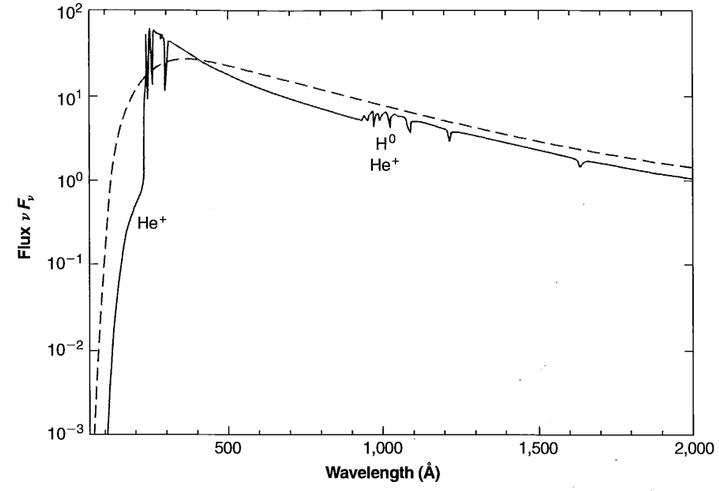

Figure 5.16
Calculated flux from a model planetary-nebula central star with $T_* = 100{,}000$ K, log $g = 6$ (*solid line*), compared with blackbody flux for the same temperature (*dashed line*). The ionization edges of atomic hydrogen and the first ion of helium are marked.

relatively unaffected by interstellar extinction, although they have the defect that this extinction enters the ratio of optical stellar flux to radio-frequency nebular flux in full force. From these measurements of about 25 nebulae, the best available model stellar atmospheres were used to derive the temperature scales for the main-sequence stars shown in Table 2.3.

In many planetary nebulae the number of ionizing photons emitted by the star beyond the He$^+$ limit can also be measured from λ4686, the strongest optical He II recombination line. This line is in general not present or only very weakly present, and has only been observed in some giant extragalactic H II regions. This indicates that the flux of He$^+$-ionizing photons is small in all main-sequence O stars, confirming the calculated models in this respect. Many of the planetary-nebula central stars, however, are considerably hotter and emit an appreciable number of photons with $h\nu > 4h\nu_0 = 54.4$ eV. Thus, from the He II observations and from Equation (2.29), we have the relation analogous to that in Equation (5.35),

$$\frac{L_{\nu_f}}{\int_{4\nu_0}^{\infty} \frac{L_\nu}{h\nu} d\nu} = h\nu_{\lambda 4686} \frac{\alpha^{eff}_{\lambda 4686}(\mathrm{He}^+, T)\pi F_{\nu_f}}{\alpha_B(\mathrm{He}^+, T)\pi F_{\lambda 4686}}. \tag{5.37}$$

Hence from the measured H I and He II line fluxes of the nebula, together with the measured stellar flux at some observable frequency, two independent determinations of T_* can be made by the Zanstra method. In some nebulae these two determinations agree, but in other nebulae they disagree badly. For instance, in NGC 7662, the H I measurements indicates $T_* = 70{,}000$ K, while the He II measurement indicates that $T_* = 113{,}000$ K, which, in fact corresponds to over 100 times more He^+-ionizing photons than does the lower temperature. The discrepancy may be understood as resulting from the fact that the nebula is not optically thick to the H-ionizing radiation as Equation (5.35) assumes. If the nebula is density-bounded rather than ionization-bounded, then we must replace Equation (5.35) with

$$\frac{L_{\nu_f}}{\int_{\nu_0}^{\infty} \frac{L_\nu}{h\nu} d\nu} = \eta_{\mathrm{H}} h\nu_{\mathrm{H}\beta} \frac{\alpha_{\mathrm{H}\beta}^{eff}(\mathrm{H}^0, T)\pi F_{\nu_f}}{\alpha_B(\mathrm{H}^0, T)\pi F_{\mathrm{H}\beta}} \tag{5.38}$$

where η_{H} represents the fraction of the H-ionizing photons that are absorbed in the nebula. Likewise it is possible to imagine that all the He^+-ionizing photons are not absorbed within the nebula—that is, that even the He^{++} zone is density-bounded rather than ionization-bounded. However, this does not seem to occur in most of the observed planetaries because nearly all observed planetaries have He I lines in their observed spectra, indicating the existence of an outer He^+ zone, which, as the discussion of Chapter 2 shows, is certainly optically thick to He^+ ionizing radiation. In a similar way, if [O I] lines are observed in a nebula, they indicate the presence of O^0, and therefore also of H^0, which has the same ionization potential as O^0, and thus indicates that the nebula is optically thick to H-ionizing radiation and that $\eta = 1$ (assuming spherical symmetry).

One further item of information can be obtained from measurements of the flux in a He I recombination line, such as λ4471 or λ5876—namely, the number of photons emitted that can ionize He^0. This condition is

$$\frac{L_{\nu_f}}{\int_{\nu_2}^{\infty} \frac{L_\nu}{h\nu} d\nu} = \eta_{\mathrm{He}} h\nu_{\lambda 5876} \frac{\alpha_{\lambda 5876}^{eff}(\mathrm{He}^0, T)\pi F_{\nu_f}}{\alpha_B(\mathrm{He}^0, T)\pi F_{\lambda 5876}}. \tag{5.39}$$

If the nebula is known to be optically thick to the He-ionizing radiation, either because the He^+ zone is observed to be smaller than the H^+ zone, or because the apparent abundance ratio $n(He^+)/n_p \leq 0.1$ (presumably indicating that the He^+ zone is smaller than the H^+ zone, even though this was not directly observed), then $\eta_{\mathrm{He}} = 1$.

It should be noted that although the integrals giving the numbers of photons that can ionize He^+, He^0, and H^0 in Equations (5.26), (5.28), and (5.27), respectively, overlap, the equations are nevertheless essentially correct, because as indicated in Chapter 2, nearly every recombination of a He^{++} ion leads to emission of a photon that can ionize He^0 or H^0, and nearly every recombination of a He^+ ion leads to emission of a photon that can ionize H^0.

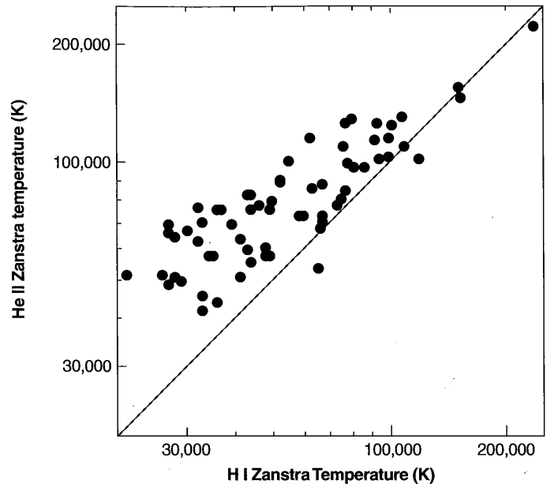

Figure 5.17
Comparison between Zanstra temperatures determined from H I and He II recombination lines.

The observational data on the fluxes in Hβ, λ4686, and λ4471 are fairly complete and fairly accurate for planetary nebulae. The measurements of the stellar continuum fluxes are less accurate, because the stars are faint and must be observed on the bright background of the nebula. The best measurements are those that avoid the wavelengths of the nebular emission lines.

Figure 5.17 compares Zanstra temperatures obtained from straightforward application of Equations (5.35) and (5.37). The He II Zanstra temperature often exceeds the H I temperature. This is generally ascribed to the nebulae being partially transparent to hydrogen-ionizing radiation, in which case the He II temperature is the more accurate value.

Another, related method of determining the temperature of the central star is to measure directly all the cooling radiation. If the fluxes in all the emission lines plus the continuum, from the ultraviolet to the infrared, are added together, this gives directly the energy radiated by the nebula. Comparing this quantity with the flux in a hydrogen recombination gives the energy radiated per recombination (through the ratio $\alpha_B/\alpha_{\mathrm{H}\beta}^{eff}$)—that is, the energy input to the nebula per photoionization.

$$\frac{\text{total cooling}}{L(\mathrm{H}\beta)} = \frac{\text{total heating}}{L(\mathrm{H}\beta)} = \frac{\alpha_B}{h\nu_{\mathrm{H}\beta}\alpha_{\mathrm{H}\beta}^{eff}} \frac{\int_{\nu_0}^{\infty} \frac{L_\nu}{h\nu} \alpha_\nu h(\nu - \nu_o)\, d\nu}{\int_{\nu_0}^{\infty} \frac{L_\nu}{h\nu} \alpha_\nu\, d\nu} \tag{5.40}$$

This can be viewed as the next higher moment of the radiation field measured by the Zanstra method, and determines the effective temperature of the star, either in the blackbody approximation, or from a series of model atmospheres. This method of temperature determination is called the energy balance or Stoy's method and, as observations into the ultraviolet and infrared spectral regions become more straightforward, it will become increasingly useful. Note that if the continuum flux is not measured, it can be estimated as the energy lost (in the Balmer, Paschen, etc., continua) by the recombining electrons as outlined in Section 3.3.

5.11 Abundances of the Elements in Nebulae

It is clear that abundances of the observed ions in nebulae can be derived from measurements of the relative strengths of their emission lines. All the individual nebular lines are optically thin, so that no curve-of-growth effects of the kind that complicate stellar atmosphere abundance determinations occur. Many light elements are observable in the optical spectra of nebulae, including H, He, N, O, and Ne, although unfortunately C is not. However, it can be observed in the satellite ultraviolet spectral region. Collisionally excited lines can be quite bright, but their strengths depend strongly on temperature, which complicates the determination of relative abundances. Furthermore, all stages of ionization of an element are generally not observable in the optical spectral region; for instance, though [O II] and [O III] have strong lines in diffuse nebulae, O IV and O V do not. However, there is an [O IV] line in the far infrared, and O IV] and O V lines in the satellite ultraviolet. Opening up these new wavelength regions has greatly aided abundance determinations.

In general, as we have seen in Chapter 4, the observed intensity I_l of an emission line is given by the integral

$$I_l = \int j_l ds = \int n_i n_e \varepsilon_l (T)\, ds \tag{5.41}$$

taken along the line of sight through the nebula, where n_i and n_e are the density of the ion responsible for the emission and the electron density, respectively.

For the recombination lines, the emission coefficients have been discussed in Chapter 4, and we have, for instance,

$$I_{\mathrm{H}\beta} = \frac{1}{4\pi} \int n_p n_e h\nu_{\mathrm{H}\beta} \alpha^{eff}_{\mathrm{H}\beta}(\mathrm{H}^0, T) ds,$$

$$I_{\lambda 5876} = \frac{1}{4\pi} \int n(\mathrm{He}^+) n_e h\nu_{\lambda 5876} \alpha^{eff}_{\lambda 5876}(\mathrm{He}^0, T) ds,$$

$$I_{\lambda 4686} = \frac{1}{4\pi} \int n(\mathrm{He}^{++}) n_e h\nu_{\lambda 4686} \alpha^{eff}_{\lambda 4686}(\mathrm{He}^+, T) ds.$$

For all the recombination lines, $\varepsilon_l \propto T^{-m}$ can be fitted over a limited range of temperature, with $m \approx 1$. For instance, for Hβ, $m = 0.90$, while for He I λ5876, $m = 1.13$. Thus the recombination-emission coefficients are not particularly temperature

sensitive and the abundances derived from them do not depend strongly on the assumed T. But their intensities scale with the abundances, making recombination lines of elements heavier than helium faint and hard to observe.

Less abundant ions, such as C II, O IV, and O V, have weak permitted emission lines as observed in planetary nebulae, and these lines have often been interpreted as resulting from recombination, and have been used to derive abundances of the parent ions. However, some of these lines may be excited by resonance–fluorescence, and their emission coefficients therefore depend not only on temperature and density but on the local radiation field as well, so they cannot be used to derive abundances in any straightforward way. Other lines, such as C II $3\,^2D$–$4\,^2F$ λ4267, cannot be excited by resonance–fluorescence, and are suitable for abundance determinations. Abundances determined from collisionally excited and recombination lines should agree, but as we shall see, there are several nebulae where they do not, and this is a current area of active research.

It is also possible to measure relative abundances of He^+ in H II regions from relative strengths of the radio recombination lines of H I and He I. At the very high n of interest in the radio region, both H and He are nearly identical one-electron systems except for their masses, so that the relative strengths of their lines (separated by the isotope effect) are directly proportional to their relative abundances as long as the lines are optically thin, and the nebula is a complete H^+, He^+ region, with no H^+, He^0 zone.

For abundance determinations of elements other than H and He, strong collisionally excited lines are available, and for these lines, in contrast to the recombination lines, the emission coefficient depends more sensitively on the temperature,

$$I_\nu = \frac{1}{4\pi} \int n_i n_e h\nu q_{1,2}(T) b\, ds$$

$$= \frac{1}{4\pi} \int n_i n_e h\nu \frac{8.63 \times 10^{-6}}{T^{1/2}} \frac{\Upsilon(1,2)}{\omega_1} \exp(-\chi/kT) b\, ds$$

in the low-density limit, where b is the fraction of excitations to level 2 that are followed by emission of a photon in the line observed.

The temperature must be determined from observational data of the kind discussed in the beginning sections of this chapter. From the measured relative strengths of the lines and the known emission coefficients, the abundances can be determined on the basis of a model of the structure of the nebula. The simplest model treats the nebula as homogeneous with constant T and n_e and thus might be called a one-layer model. From each observed relative line strength, the abundance of the ion that emits it can be determined. In some cases two successive stages of ionization of the same element are observed, such as O^+ and O^{++}, and their relative abundances can be used to construct an empirical ionization curve giving $n(A^{+m+1})/n(A^{+m})$ as a function of ionization potential. Thus finally, the relative abundance of every element with at least one observed line can be determined. Discrepancies (for instance, in n_e and T) determined from different line ratios indicate that this model is too simplified to

give highly accurate results, though the abundances determined from it are generally thought to be correct to within a factor of order two or three.

Previous sections have described several methods of determining the temperature, and the discussion has shown that temperatures determined from hydrogen recombination lines, the Balmer jump, and free–free brightness temperatures are lower than the temperature determined from forbidden-line ratios. The probable explanation of this discrepancy is that the temperature is not constant throughout the nebula as has been tacitly assumed, but rather varies from point to point due to variations in the local heating and cooling rates. Under this interpretation, a more complicated comparison between observation and theory is necessary. An ideal method would be to know the entire temperature structure of the nebula, to calculate from it the expected forbidden-line ratios and radio-frequency continuum brightness temperatures, and then to compare them with observation; this is a model approach that will be discussed in Section 5.12.

However, the general type of effects that are expected can easily be understood. The forbidden-line ratios determine the temperature in the region in which these lines themselves are emitted—that is, the [O III] ratio measures a mean temperature in the O^{++} zone and the [N II] ratio measures the mean temperature weighted in a different way. The emission coefficient for the forbidden lines increases strongly with increasing temperature, and therefore the mean they measure is strongly weighted toward high-temperature regions. On the other hand, the recombination and free–free emission coefficients decrease with increasing temperature, and therefore the mean it measures is weighted toward low-temperature regions. We thus expect a discrepancy in the sense that the forbidden lines indicate a higher temperature than do the Balmer jump or radio-frequency measurements, as is in fact confirmed by observation. It is even possible to get some information about the range in variation of the temperature along a line through the nebula from comparison of these various temperatures, but as the result depends on the ionization distribution also, we shall not consider this method in detail.

A somewhat more sophisticated scheme takes into account the spatial variations of temperature along the line of sight and uses the observations themselves to get as much information as possible on these variations. The emission coefficient is expanded in a power series,

$$\varepsilon_l(T) = \varepsilon_l(T_0) + (T - T_0)\left(\frac{d\varepsilon_l}{dT}\right)_0 + \frac{1}{2}(T - T_0)^2\left(\frac{d^2\varepsilon_l}{dT^2}\right)_0, \tag{5.42}$$

correct to the second order. It is clear that for recombination lines with

$$\varepsilon_l(T) = CT^{-m}$$

or for collisionally excited lines with

$$\varepsilon_l(T) = \frac{D\exp(-\chi/kT)}{T^{1/2}},$$

(in the low-density limit) the necessary derivatives can be worked out analytically. Then, integrating along the line of sight,

$$\int n_i n_e \varepsilon_l(T)ds = \varepsilon_l(T_0)\int n_i n_e ds + \frac{1}{2}\left(\frac{d^2\varepsilon_l}{dT^2}\right)_0 \int n_i n_e (T - T_0)^2 ds \tag{5.43}$$

where T_0 is chosen so that

$$T_0 = \frac{\int n_i n_e T\, ds}{\int n_i n_e ds}. \tag{5.44}$$

If all ions had the same space distribution $n_i(s)$, then from two line ratios, such as [O III] (λ4959 + λ5007)/λ4363 and [N II] (λ6548 + λ6583)/λ5755, both T_0 and

$$t^2 = \frac{\int n_i n_e (T - T_0)^2 ds}{T_0^2 \int n_i n_e ds}$$

could be determined instead of the one constant T_0 from one line ratio, as in the single-layer model. Then T_0 and t^2 could be used to determine the abundances of all the ions with measured lines. The difficulty with this method is that all ions do not have the same distribution; for instance, O^{++} is more strongly concentrated to the source of ionizing radiation than N^+, so other more or less arbitrary assumptions must be made.

The most sophisticated method of all to determine the abundances from the observations is to calculate a complete model of the nebula in an attempt to reproduce all its observed properties; this approach will be discussed in the next section.

Turning now to the observational results, the He/H abundance ratio has been measured in many nebulae. Perhaps the most exhaustively measured nebula is the Orion Nebula, which has He I but not He II lines. Observations show that $n(He^+)/n_p$ ranges from 0.060 to 0.090 in various positions, suggesting that varying amounts of He^0 are present. A measurement in its nearby companion nebula NGC 1982 gives $n(He^+)/n_p = 0.009$ and definitely shows that this slit position is in an H^+, He^0 zone where He is neutral. The exciting star of NGC 1982 is a B1 V star, so the fact that the nebula is a He^0 zone is understood from Figure 2.5. This observation shows that some correction of the abundance of He for the unobserved He^0 is probably necessary at all the observed slit positions in the Orion Nebula.

Atomic helium produces no emission lines, so an ion of another element is used as its proxy. Empirically, the correction can be based on the observed strength of [S II] $\lambda\lambda$6717, 6731, because their emitting ion S^+ has an ionization potential of 23.4 eV,

approximately the same as the ionization potential of He^0, 24.6 eV, so that to a first approximation

$$\frac{n(He^0)}{n(He^+)} = \frac{n(S^+)}{n(S^{++})}$$

yields the abundance of He^0. Such ratios are often called "ionization correction factors" (ICF), since they apply a correction for unobserved stages of ionization. A more sophisticated procedure is to obtain the ICF by interpolation between the ionization of S^+ and of O^+ (ionization potential 35.1 eV) in such a way that the corrections at all slit positions yield as nearly as possible the same final He/H ratio. The final result for NGC 1976 is $n(He)/n(H) \approx 0.10$; two other H II regions observed optically, M 8 and M 17, have essentially this same relative He abundance.

Radio measurements of He^+/H^+ abundance ratios are available for many diffuse nebulae. These determinations have the advantage that they can be done at great distances within the galactic plane, where extinction is large in the optical, and they are in good agreement with the optical measurement for nebulae common to both sets of observations. At present, however, there is no known way in which the correction for He^0 can be obtained from radio measurements alone, and the fact that at least two nebulae, NGC 2024 and NGC 1982, are observed to have $n(He^+)/n_p \approx 0$ shows that this correction certainly exists. Radio measurements of H II regions very near the galactic center give quite low $n(He^+)/n_p$ ratios, but it appears most likely that they indicate that the ionizing stars are predominantly rather cool, producing H^+, He^0 zones, rather than low helium abundance.

Both He II and He I recombination lines are observed in many planetary nebulae, showing the presence of both He^{++} and He^+, though some planetaries, like H II regions, have only He I lines. Nearly all planetaries have central stars that are so hot that they have no outer H^+, He^0 zones, though a few exceptions do exist. Thus no correction is necessary for unobserved He^0 in most planetary nebulae.

Accurate measurements of He abundances of planetary nebulae show that most have values only slightly above H II regions, with $n(He)/n(H) \approx 0.11$. However some nebulae have abundances that are almost twice as large. Since the accuracy of the measurements, as judged from the relative intensities of He I λλ4471, 5876, is about 0.01, the differences between the nebulae are real. As will be discussed in Chapter 11, the helium abundance can help distinguish between different populations of planetary nebulae.

Most measurements of the abundances of the heavy elements in H II regions and planetary nebulae use a combination of collisionally excited forbidden lines and hydrogen recombination lines. Section 5.10 shows that the intensities of forbidden lines relative to a recombination line depend mainly on the shape of the stellar continuum [Equation (5.40)]. Physically, the gas will be hotter in lower-metallicty nebulae, to compensate for the fewer number of coolants, and the result will be that the sum of the collisionally excited lines, which represent the majority of the cooling, is constant. Forbidden lines can only be converted into abundances if the electron temperature is well measured, which requires detection of the faint ^1S–^1D transitions described in Section 5.2. A second difficulty is that large and rather uncertain corrections may be

Table 5.3
Abundances of the elements

N	Atom	Sun	H II Region	Planetary
1	H	1	1	1
2	He	0.1	0.095	0.10
6	C	3.5×10^{-4}	3×10^{-4}	8×10^{-4}
7	N	9.3×10^{-5}	7×10^{-5}	2×10^{-4}
8	O	7.4×10^{-4}	4×10^{-4}	4×10^{-4}
10	Ne	1.2×10^{-4}	6×10^{-5}	1×10^{-4}
11	Na	2.1×10^{-6}	3×10^{-7}	2×10^{-6}
12	Mg	3.8×10^{-5}	3×10^{-6}	2×10^{-6}
13	Al	2.9×10^{-6}	2×10^{-7}	3×10^{-7}
14	Si	3.6×10^{-5}	4×10^{-6}	1×10^{-5}
16	S	1.6×10^{-5}	1×10^{-5}	1×10^{-5}
17	Cl	1.9×10^{-7}	1×10^{-7}	2×10^{-7}
18	Ar	4.0×10^{-6}	3×10^{-6}	3×10^{-6}
19	K	1.3×10^{-7}	1×10^{-8}	1×10^{-7}
20	Ca	2.3×10^{-6}	2×10^{-8}	1×10^{-8}
26	Fe	3.2×10^{-5}	3×10^{-6}	5×10^{-7}

required for unseen ions—that is, ions without observable lines—unless co-spatial ultraviolet, optical, and infrared measurements are available.

Table 5.3 summarizes the abundances of the more common elements for the sun, NGC 1976, and the mean of a sample of planetary nebulae. These are only given as indicators of typical values, and we shall see in Chapters 10 and 11 that there is a dispersion in observed abundances. The abundances of a particular planetary nebula are affected by nuclear processing in the central star, or the abundances in an H II region reflect the composition of the interstellar medium in that part of the galaxy. Also, as we shall see in Chapter 7, certain elements, especially Ca and Al, have condensed onto grains and so are not included in the emission-line abundances.

Large telescopes and efficient CCD detectors have made it possible to detect faint recombination lines of the heavy elements in several H II regions and planetary nebulae. Abundances measured with these should be far more robust than those inferred from the bright forbidden lines, because both heavy-element and hydrogen recombination lines have similar temperature dependencies, which then cancel in the ratio. In particular, this method should not be affected by temperature fluctuations. This advantage is mitigated by the fact that the lines are faint, and the recombination process is complicated by strong dielectronic recombination contributions.

Among H II regions the recombination-line abundances tend to be slightly higher than the forbidden-line abundances, which can be understood in terms of the temperature fluctuations described in the first parts of this section. If this is the correct

interpretation then the correct gas-phase abundances are about 50%–100% higher than are given in Table 5.3 and $t^2 \sim 0.02$–0.04.

Recent work on planetary nebulae has found differences between collisional and recombination abundances that are larger than a factor of ten, too large to be caused by temperature fluctuations. This suggests that another, presently unknown, process may be affecting one (or both) of the abundance measures. The fact that the discrepancy is not constant, but varies from object to object, shows that it is not a simple matter of incorrect atomic data. One study finds a correlation between t^2 (measured from the forbidden-line/Balmer-jump method) and the difference between the collisional and recombination abundances, suggesting that the difference is related to physical conditions within the nebulae. If this is the case then the higher recombination abundances are more likely to be correct. Another study shows that, across the planetary nebula NGC 6720, the recombination line abundances measured in low- and high-ionization regions are quite different, while collisionally excited lines indicate a consistent oxygen abundance. This suggests that an unknown process affects the recombination lines in the higher-ionization gas. This is clearly an active research area, with major consequences for galactic chemical evolution.

5.12 Calculations of the Structure of Model Nebulae

The basic idea of a calculation of a model H II region or a model planetary nebula is quite straightforward. It is to make reasonable assumptions about the physical parameters of the ionizing star, the density distribution, and the relative abundances of the elements in the nebula (its size, geometrical structure, and so on); to calculate, on the basis of these assumptions, the resulting complete physical structure—the ionization, temperature, and emission coefficients as functions of position; and thus to calculate the expected emergent radiation from the nebula at each point in each emission line. Comparing this predicted model with the observed properties of a nebula provides a check as to whether the initial assumptions are consistent with the observations; if they are not, then the assumptions must be varied until a match with the observational data is obtained. In principle, if all the emission lines were accurately measured at every point in the nebula, and if the central star's radiation were measured at each observable frequency, it might be possible to specify accurately all the properties of the star and of the nebula in this way. Of course, in practice the observations are not sufficiently complete and accurate, and do not have sufficiently high angular resolution to enable us to carry out this ambitious program, but nevertheless, quite important information is derived from the model-nebula calculation.

Let us write down in simplified form the equations used in calculating the structure of a model nebula. For computational reasons, practically all work to date has assumed spherical model nebulae, and we shall write the equation in these terms. The basic equations are described in Chapters 2 and 3, so we shall simply quote them here. The basic equation of transfer is

$$\frac{dI_\nu}{ds} = -\frac{d\tau_\nu}{ds} I_\nu + j_\nu \tag{5.45}$$

where the increment in optical depth at any frequency is given by a sum

$$\frac{d\tau_\nu}{ds} = \sum n_j a_{\nu j} \tag{5.46}$$

over all atoms and ions with ionization potentials $h\nu_j < h\nu$. In practice, because of their great abundance, H^0, He^0, and He^+ dominate the total opacity, although all ions are included in the optical depth. Likewise, the emission coefficient j_ν is a sum of terms of which those due to recombinations of H^+, He^+, and He^{++} are the most important.

The ionization equation that applies between any two successive stages of ionization of any ion is

$$n(X^{+i}) \int_{\nu_o}^{\infty} \frac{4\pi J_\nu}{h\nu} a_\nu(X^{+i}) d\nu = n(X^{+i}) n_e \alpha_G(X^{+i+1}, T) \tag{5.47}$$

as in Equation (2.30), while the total number of ions in all stages of ionization is

$$\sum_{i=0}^{\max} n(X^{+i}) = n(X)$$

The energy-equilibrium equation is

$$G = L_R + L_{FF} + L_C \tag{5.48}$$

as in Equation (3.33), where the gain term and each of the loss terms is a sum over the contributions of all ions, but again in practice usually only H and He are important in L_R and L_{FF}. Collisionally excited line radiation from the less abundant heavy elements dominates the cooling, however, and many terms must be included in L_C.

For any assumed radiation source at the origin, taken to be a star with either a blackbody spectrum, or a spectrum calculated from a model stellar atmosphere, these equations can be integrated. If the on-the-spot approximation described in Chapter 2 is used, they can be integrated outward. If, instead, the detailed expressions for the emission coefficients are used and the diffuse radiation field is explicitly calculated, it is necessary to use an iterative procedure. The on-the-spot approximation can be used as a first approximation from which the ionization at each point in the nebula and the resulting emission coefficients can be calculated. Then the diffuse radiation field can be calculated working outward from the origin, and using the then more nearly accurate total radiation field, the ionization and T can be recalculated at each point. This process can be repeated as many times as needed until it converges to the desired accuracy.

As an example, we shall examine a reconstruction of the geometry and physical properties of the planetary nebula NGC 6565, a bright, compact object that appears as a homogeneous oval ring when imaged in [O III], as shown in Figure 5.18. A long slit was placed across the nebula to obtain spatially resolved spectra at a resolving power

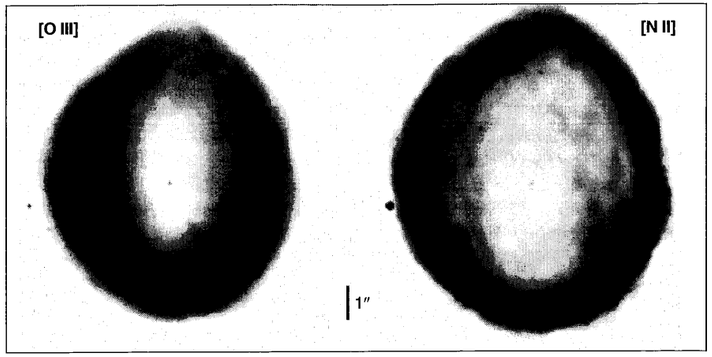

Figure 5.18
HST images of NGC 6565 in [O III] (left) and [N II] (right). The vertical bar indicates 1″.

of 60,000. This was done at a series of position angles to measure the expansion velocity and distribution of ions across the nebula. As is typical of planetary nebulae, a wide range of ionization ([N I] through [Ar V]) and expansion velocity (70 km s^{-1} through ~17 km s^{-1}) was seen.

The ionization structure and nebular properties were deduced by combining the spatially resolved spectroscopy with photoionization models. The gas density was deduced from the surface brightness in Hα, which is proportional to $n_e n_p L$, where L is the physical thickness. The density distribution was found to be radially asymmetric, with a peak ~3″ away from the star, but with greater emission on the side of the peak towards the central star. The gas filling factor, deduced from the physical arguments presented above, was ~0.25. The gas temperature as a function of radius was determined, for several ions, by the methods described in Section 5.2. The central star temperature was deduced to be between 1.2×10^5 K and 1.6×10^5 K from the Zanstra method.

The ionization and thermal structure of the nebula was reproduced with a photoionization model, which included the effects of embedded dust and used the deduced density profile. It was adjusted to reproduce the observed spatial distribution of ionization of the elements, surface brightnesses of several lines, and the measured temperature. A blackbody at ~1.2×10^5 K, with a luminosity of 100 $L_\odot$, was deduced, along with the chemical composition of the gas, and the three-dimensional geometry of the nebula. The composition was typical of planetary nebulae. Figure 5.19 shows the three-dimensional reconstructed geometry.

Photoionization models have also been created to fit observations of H II regions. As we shall see in Chapter 10, an H II region is an illuminated layer of ionized gas on the surface of a much larger molecular cloud. As an example we will consider a model of inner regions of NGC 1976. The H II region is treated as a hydrostatic layer with the gas in overall pressure equilibrium. An ionizing continuum predicted

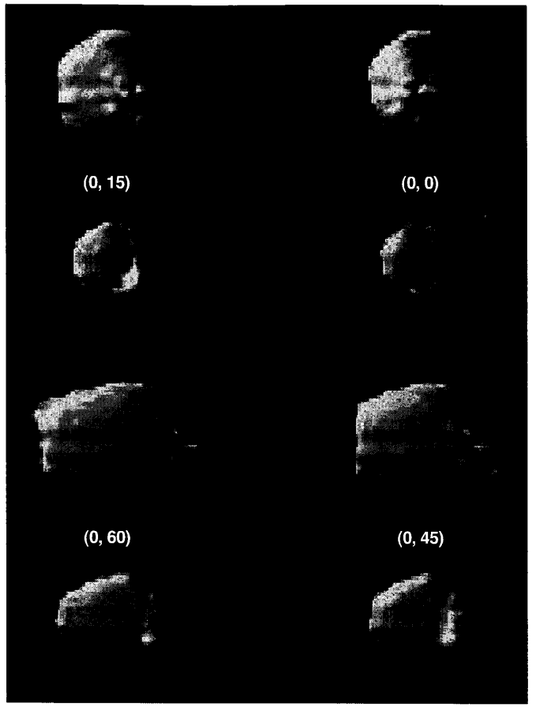

Figure 5.19
The three-dimensional reconstructed geometry of NGC 6565. Each pair of images should be viewed with the left and right eye to see the deduced three-dimensional structure.

by stellar atmospheres was assumed, and a temperature of ~39,600 K was deduced. Grains, and their effects on the extinction of the stellar continuum, the heating of the gas by photoionization, and the observed grain thermal emission, were included in the calculation. The deduced composition was similar to that given in Table 5.3.

References

An old but very good overall reference on the comparison of theory and observation of the optical radiation of nebulae, written in the context of planetary nebulae, but applicable in many ways to H II regions also, is

Seaton, M. J. 1960, Rep Progress in Phys, 23, 313.

The method of measuring electron temperatures from optical emission-line intensity ratios seems to have been first suggested by

Menzel, D. H., Aller, L. H., & Hebb, M. H. 1941, ApJ, 93, 230.

This method has subsequently been used by many authors.

The observational data used in Figure 5.2 are from

Garnett, D. R., Shields, G. A., Skillman, E. D., Sagan, S. P., & Dufour, R. J. 1997, ApJ, 489, 63 (NGC 2403).

Kennicutt, R. C., Bresolin, F., & Garnett, D. R. 2003, ApJ, 591, 801 (M101).

Osterbrock, D. E., Tran, H. D., & Veilleux, S. 1992, ApJ, 389, 305 (Orion).

Esteban, C., Peimbert, M., Torres-Peimbert, S., & Escalante, V. 1998, MNRAS, 295, 401 (Orion).

The observational data used in Figure 5.3 are from

Kwitter, K. B., & Henry, R. B. C. 2001, ApJ, 562, 804 (filled circles).

Milingo, J. B., Henry, R. B. C., & Kwitter, K. B. 2002, ApJS, 138, 285 (filled circles).

Kingsurgh, R. L., & Barlow, M. J. 1994, MNRAS, 271, 257 (open circles).

The C III] λ1909/C II λ4267 ratio method is described by

Kaler, J. B. 1986, ApJ, 308, 337.

The curves in Figure 5.4 were computed by combining collision strengths from the Chapter 3 with recombination rate coefficients from the following references:

Davey, A. R., Storey, P. J., & Kisielius, R. 2000, A&A, 142, 85.

Kisielius, R., & Storey, P. J. 1999, A&AS, 137, 157.

Storey, P. J. 1994, A&A, 282, 999.

The observational data for the optical continuum temperature determinations of Figure 5.6 are from

Liu, X.-w., & Danziger, J. 1993, MNRAS, 262, 256, and papers cited therein.

The radio-continuum method of measuring the temperature of a nebula by observing it in the optically thick region has been discussed and used by many authors. The numerical data on which Table 5.1 is based are from

Subrahmanyan, R., & Goss, W. M. 1996, MNRAS, 281, 239.

Subrahmanyan, R., & Goss, W. M. 1995, MNRAS, 275, 755.

Subrahmanyan, R. 1992, MNRAS, 254, 719.

Shaver, P. A. 1970, Ap. Letters, 5, 167.

The first paper is a good review of excitation processes that determine the populations of the hyperfine structure levels of H I, and gives references to the atomic data. The second paper applies the radio/UV line method to the Orion environment.

Liszt, H. 2001, A&A, 371, 698.

van der Werf, P. P., & Goss, W. M. 1989, A&A, 224, 209.

The idea of using the [O II] intensity ratio to measure electron densities in nebulae seems to have been first suggested by

Aller, L. H., Ufford, C. W., & Van Vleck, J. H. 1949, ApJ, 109, 42.

It was worked out quantitatively by

Seaton, M. J. 1954, Ann. d'Ap, 17, 74.

A complete discussion, including theoretical calculations and observational data on several of the H II regions used in Table 5.6, is found in

Seaton, M. J., & Osterbrock, D. E. 1957, ApJ, 125, 66.

For many years a discrepancy existed between the calculated transition probabilities for the np^3 ions like [O II] and [S II] on which nebular electron-density determinations depend, and the values implied by the astronomical data. This discrepancy was finally resolved by the realization that a full relativistic quantum-mechanical treatment, including Dirac relativistic wave functions and the relativistic corrections to the magnetic-dipole operator, is necessary to calculate accurately the transition probabilities for these ions. Relevant references are

Eissner, W., & Zeippen C. J. 1981, J. Phys. B, 14, 2125.

Zeippen, C. J. 1982, MNRAS, 198, 111.

Mendoza, C. & Zeippen, C. J. 1982, MNRAS, 199, 1025.

Zeippen, C. J. 1987, A&A, 173, 410.

An extensive comparison between various density indicators is presented by

Copetti, M. V. F., & Writzl, B. C. 2002, A&A, 382, 282.

The data shown in Figure 5.9 are from

Kingburgh, R. L., & English, J. 1992, MNRAS, 259, 635.

The observational data in Table 5.2 are from

Osterbrock, D. E., & Flather, E. 1959, ApJ, 129, 26 (NGC 1976).

Meaburn, J. 1969, Astron. Space Science, 3, 600 (M 8).

Danks, A. C. 1970, A&A, 9, 175 [S II].

Danks, A. C., & Meaburn, J. 1971, Astron. Space Science, 11, 398 (NGC 1976).

Esteban, C., Peimbert, M., Torres-Peimbert, S., Garcia-Rojas, J., & Rodriguez, M. 1999, ApJS, 120, 113 (M 8).

A very good reference to the simultaneous determination of temperature and density by comparison of optical and infrared emission line strengths is

Dinerstein, H. L., Lester, D. F., & Werner, M. W. 1985, ApJ, 291, 561.

The data shown in Figure 5.12 are taken from this reference.

Comparison of radio-recombination-line measurements with calculated strengths and the determination of T, n_e and E have been investigated by many authors, beginning with

Goldberg, L. 1966, ApJ, 144, 1225.

Mezger, P. G., & Hoglund, B. 1967, ApJ, 147, 490.

Dyson, J. E. 1967, ApJ, 150, L45.

Note, however, that the definition of β used in the present text differs slightly from that used in most of these papers. The more recent results are taken from

Brown, R. L., Lockman, F. J., & Knapp, G. R. 1978, ARAA, 16, 445.

Shaver, P. A. 1980, A&A, 91, 279.

Odegard, N. 1985, ApJS, 57, 571.

Shaver, P. A., McGee, R. X., Newton, L. M., Danks, A. C., & Pottasch, S. R. 1983, MNRAS, 204, 53.

Figure 5.14 uses data from the last of these references.

The method of measuring the ultraviolet radiation of stars from the recombination radiation of the nebulae they ionize was first suggested by

Zanstra, H. 1931, Pub. Dominion Astrophys. Obs, 4, 209.

The treatment in this chapter is based primarily on the following paper, which includes the best available optical- and radio-frequency measurements:

Harman, R. J., & Seaton, M. J. 1966, MNRAS, 132, 15.

The following give tables of emergent continua for OB stars (the first two) and for nuclei of planetary nebulae (the last):

Kurucz, R. L. 1991, in *Proceedings of the Workshop on Precision Photometry: Astrophysics of the Galaxy*, ed. A. C. Davis Philip, A. R. Upgren, & K. A. James (Schenectady: Davis), p. 27. On the web at *http://www.stsci.edu/science/starburst/Kurucz.html*.

Schaerer D., & de Koter, A. 1997, A&A, 322, 592. On the web at *http://www.stsci.edu/ftp/science/starburst/SdK96.html*.

Rauch, T. 1997, A&A, 320, 237. On the web at *http://astro.uni-tuebingen.de/~rauch/flux.html*.

The stellar atmosphere used in Figure 5.15 was taken from the first of these references, and the planetary nebula atmosphere from the last.

This paper contains good tables of the left-hand sides of Equations (5.33) and (5.35) for many published model stellar atmospheres.

Shaw, R. A., & Kaler, J. B. 1985, ApJ, 295, 537.

This reference contains the best magnitudes of the central stars of planetary nebulae, measured with narrow-band filters at λ4428 and λ5500, between the strong nebular lines, and corrected for contamination by the nebular continuum. Blackbody temperature determinations from it are used in preference to earlier results in Table 5.10.

Figure 5.17 uses data from the following reference:

Gleizes, F., Ackler, A., & Stenholm, B. 1989, A&A, 222, 237.

These three references describe and apply the Stoy method for temperature determination:

Stoy, R. H. 1933, MNRAS, 93, 588.

Kaler, J. B. 1976, ApJ, 210, 843.

Kaler, J. B. 1978, ApJ, 220, 887.

Recent surveys of abundance determinations in H II regions include

Rubin, R. H., Simpson, J. P., Haas, M. R., & Erickson, E. F. 1991, ApJ, 374, 564.

Baldwin, J., Ferland, G. J., Martin, P. G., Corbin, M., Cota, S., Peterson, B. M., & Slettebak, A. 1991, ApJ, 374, 580.

Osterbrock, D. E., Tran, H. D., & Veilleux, S. 1992, ApJ, 389, 305.

Esteban, C., Peimbert, M., Torres-Peimbert, S., & Escalante, V. 1998, MNRAS, 295, 401.

Deharveng, L., Peña, M., Caplan, J., & Costero, R. 2000, MNRAS, 311, 329.

The first four of these deals with NGC 1976, the best studied H II region, and all the others are on planetary nebulae.

The following paper reviews methods of deriving abundances from emission lines observed in H II regions and planetary nebulae:

Stasińska, G. 2004, in *Cosmochemistry: The Melting Pot of the Elements*, eds. C. Esteban, R. G. López, A. Herrero, & F. Sánchez (Cambridge: Cambridge University Press), p. 115, astro-ph 0207500.

Among the many discussions of complete models of planetary nebulae, some of the best are

Harrington, J. P., Seaton, M. J., Adams, P. S., & Lutz, J. H. 1982, MNRAS, 199, 517.

Clegg, R. E. S., Harrington, J. P., Barlow, M. J., & Walsh, J. R. 1987, ApJ, 314, 551.

Middlemass, D. 1990, MNRAS, 244, 294.

Volk, K., & Kwok, S. 1997, ApJ, 477, 722.

Dudziak, G., Pequignot, D., Zijlstra, A. A., & Walsh, J. R. 2000, A&A, 363, 717.

Turatto, M., Cappellera, E., Ragazzoni, R., Benetti, S., & Sabbadin, F. 2002, A&A, 384, 1062.

Figures 5.18 and 5.19 are from the last of these, along with the discussion on planetary nebula modeling in Section 5.12.

Model H II regions are discussed in

Rubin, R. H. 1983, ApJ, 274, 671.

Mathis, J. S. 1985, ApJ, 291, 247.

Rubin, R. H. 1985, ApJS, 57, 349.

Evans, I. N., & Dopita, M. A. 1985, ApJS, 58, 125.

Simpson, J. P., Rubin, R. H., Erickson, E. F., & Haas, M. R. 1986, ApJ, 311, 895.

Rubin, R. H., Simpson, J. P., Haas, M. R., & Erickson, E. F. 1991, ApJ, 374, 564.

Baldwin, J., Ferland, G. J., Martin, P. G., Corbin, M., Cota, S., Peterson, B. M., & Slettebak, A. 1991, ApJ, 374, 580.

The model of the Orion Nebula described in Section 5.12 is from the last of these.

The following paper discusses in detail corrections of the abundance ratios for unobserved stages of ionization, such as He^0, from S^+/S^{++} and O^+/O^{++} ratios, as does the earlier paper:

Mathis, J. S. 1982, ApJ, 261, 195.

The filling-factor concept was stated and applied to the analysis of observational data by

Strömgren, B. 1948, ApJ, 108, 242.

Osterbrock, D. E., & Flather, E. 1959, ApJ, 129, 26.

Recent papers that compare collisional and recombination abundances in planetary nebulae are

Garnett, D. R., & Dinerstein, H. L. 2001, ApJ, 558, 145.

Liu, X.-w., Luo, S. G., Barlow, M. J., Danziger, I. J., & Storey, P. J. 2001, MNRAS, 317, 141.

Peimbert, M., Peimbert, A., Ruiz, M. T., & Esteban, C. 2004, ApJS, 150, 431.

A recent review on t^2 in nebulae:

Peimbert, M., & Peimbert, A. 2002, Rev Mex AA 14, 47 (astro-ph 0204087).

A recent paper on the [O II] collision strengths, which resolves a controversy over their scaling for members of the multiplet, is Kisielius, Storey, Ferland & Keenan, 2009, MNRAS, 397, 903. This paper confirms the statistical weight scaling adopted by Seaton & Osterbrock (1957, ApJ, 125, 66).

6

Internal Dynamics of Gaseous Nebulae

6.1 Introduction

The first five chapters of this book have described gaseous nebulae entirely from a static point of view. However, this description is not complete, because nebulae certainly have internal motions, and the effects of these motions on their structures cannot be ignored. It is easy to see that an ionized nebula cannot be in static equilibrium, for if it is matter-bounded, it will expand into the surrounding vacuum, while if it is ionization-bounded, the hot ionized gas (with $T \approx 10{,}000$ K) will initially have a higher pressure than the surrounding cooler neutral gas ($T \approx 100$ K) and will therefore tend to expand until its density is low enough so that the pressures of the two gases are in equilibrium. In addition, when the hot star in a nebula forms and the source of the ionizing radiation is thus "turned on", the ionized volume initially grows in size at a rate fixed by the rate of emission of ionizing photons, and an ionization front separating the ionized and neutral regions propagates into the neutral gas.

Observations agree in showing that the internal velocities of nebulae are not everywhere zero. Measured radial velocities show that planetary nebulae are expanding more or less radially; mean expansion velocities are of order 25 km s^{-1}, and the velocity gradient is positive outward. Many H II regions are observed to have complex internal velocity distributions that can best be described as turbulent.

This chapter will therefore concentrate on the internal dynamics of nebulae. First it considers the hydrodynamic equations of motion that are applicable to nebulae. This discussion leads to a study of ionization fronts and of shock fronts that are generated in an expanding, predominantly photoionized, nebula. Then the available theoretical results for planetary nebulae and H II regions are analyzed. Finally, a brief synopsis of the available observational material is given, and it will be seen that more theoretical work is necessary before the observations can be fully understood, but that progress has been made in understanding some of the complications present in nature.